Universiteit Utrecht

Faculty of Science

Faculty of Geosciences

Inverse theory in paleomagnetism

Bachelor Thesis

Annemarie Koop

Mathematics // Earth Sciences

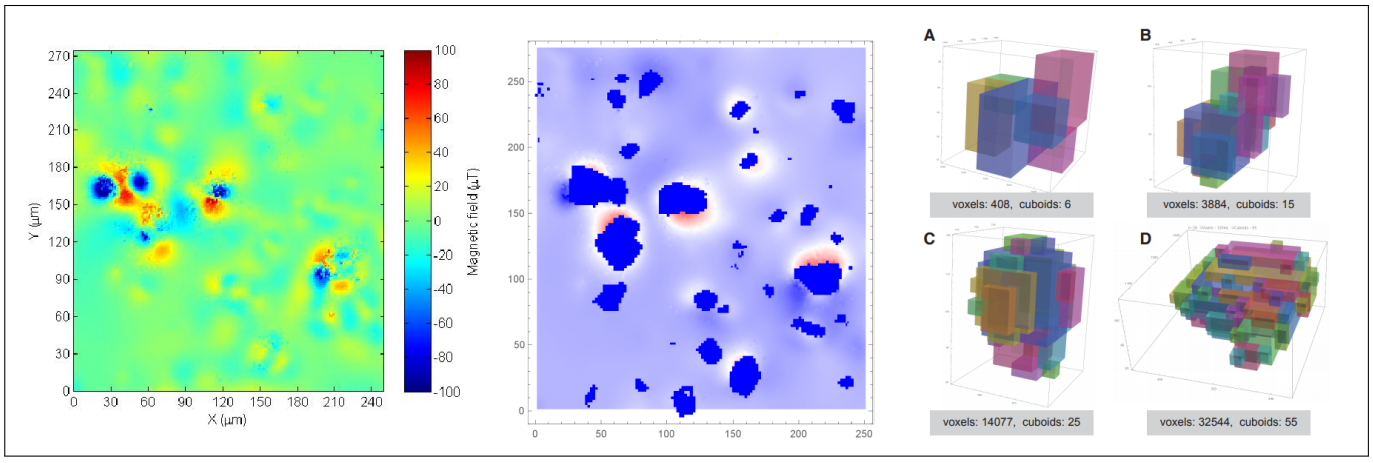

Supervisors:

Dr. van Leeuwen
Mathematical Institute

Dr. de Groot
Department of Earth Sciences

June 10, 2018

Abstract

In the field of paleomagnetism, a technique called micromagnetic tomography is developed to determine the magnetizations of individual particles in magnetic rock (A. Béguin, 2016 and de Groot et. al, 2018). Micromagnetic tomography applies an inversion to a combined data set of information on the locations and shapes of magnetic particles in a sample of magnetic rock and measurements of the magnetic flux density at the surface of that sample. The result of the inversion is the magnetization per particle. A. Béguin (2016) successfully inverted magnetizations of magnetic grains in a synthetic sample. Here, inverse theory is explained and magnetizations of magnetic grains in a natural sample of lava are inverted. About half of the magnetizations of the inversion result are unrealistically high, which seem to be the small particles and particles which are overlapped vertically by other particles. The latter is backed up by creating simple models in Matlab and examining the condition number and covariance matrix. It appears the covariance matrix can be used to detect unreliable particles before inversion.

Contents

1 Introduction

> "The geomagnetic field acts both as an umbrella, shielding us from cosmic radiation and as a window, offering one of the few glimpses of the inner workings of the Earth. Ancient records of the geomagnetic field can inform us about geodynamics of the early Earth and changes in boundary conditions through time."[12]

Research on the ancient records of the geomagnetic field is done in the field of paleomagnetism. In paleomagnetic research, the magnetic properties of a magnetized rock such as lava are examined by measuring flux of bulk samples. These measurements do not take into account that a wide variety of magnetic particles is present in the rock sample. Some of those behave unreliably with respect to magnetization, contaminating the measurements. In order to filter out unwanted particles, magnetizations of individual magnetic particles need to be established. A new technique called micromagnetic tomography offers a solution for this [2].
With micromagnetic tomography, data on the locations, sizes and shapes of particles and data on the magnetic flux density of a rock sample are assembled, after which the magnetization vector per particle can be determined with an inversion scheme. For a synthetic sample, this inversion successfully generated these magnetizations [2]. The next step is to apply it on data of a natural sample of magnetic rock.

In this thesis, we start in chapter 2 with explaining the method that leads to the mathematical model used for inversion. The model leads to a linear inverse problem, which is discussed in chapter 3: we examine existence and uniqueness of solutions in inverse theory with Singular Value Decomposition, the pseudo-inverse and the least squares solution. We look at a measurement error in our results and both the sensitivity of the solution and the associations between magnetization-components. These are represented by the condition number and covariance matrix respectively. With a Matlab-code, simple situations of magnetic particles beneath a grid of sensors are modeled, exploring the condition number and covariance matrix. In chapter 4, we gather the necessary data for inversion of a natural sample of lava and use inversion to determine the magnetizations of individual particles in the sample. Chapter 5 examines these results, looking for relations and conclusions.

2 Method

As discussed in the introduction, the aim is to determine the individual magnetizations of magnetic grains in a sample of magnetic rock. This chapter describes the method used to gather the necessary data on the magnetic flux of a magnetic particle. We start by describing how the flux of a magnetic cuboid is measured and what information on the cuboid is needed for this. We expand with describing how the measurements change when we have more cuboids contributing to the flux. Then, we elaborate on the case of multiple (not cuboid-shaped) magnetic particles, which would be the situation with a natural sample of magnetic rock. Also, we add multiple measurement points to that situation. In the end, we find a model with which we can further the search for the individual magnetizations in chapter 3.
This chapter is based on the supporting materials of de Groot et al. (2018). In these materials, the scanner used for flux measurements is a Superconducting Quantum Interference Device (SQUID) Microscope. The description of the way the flux is measured in the following sections therefore applies to this scanning device.

2.1 Measuring flux of one magnetic cuboid

We consider a cuboid-shaped particle with magnetization $\boldsymbol{M} = (m_x, m_y, m_z)$ which we assume to be homogeneous. Its edges measure $2a, 2b$ and $2c$ and it has center $\rho = (\xi, \eta, \zeta)$, we call the total border of the cuboid ∂C. The cuboid is aligned with the coordinate system. We have a rectangular sensor ∂S in the $x-y$-plane, with sides measuring $2\Delta x$ and $2\Delta y$ and center $\rho_s = (\xi_s, \eta_s, \zeta_s)$. See figure 1.

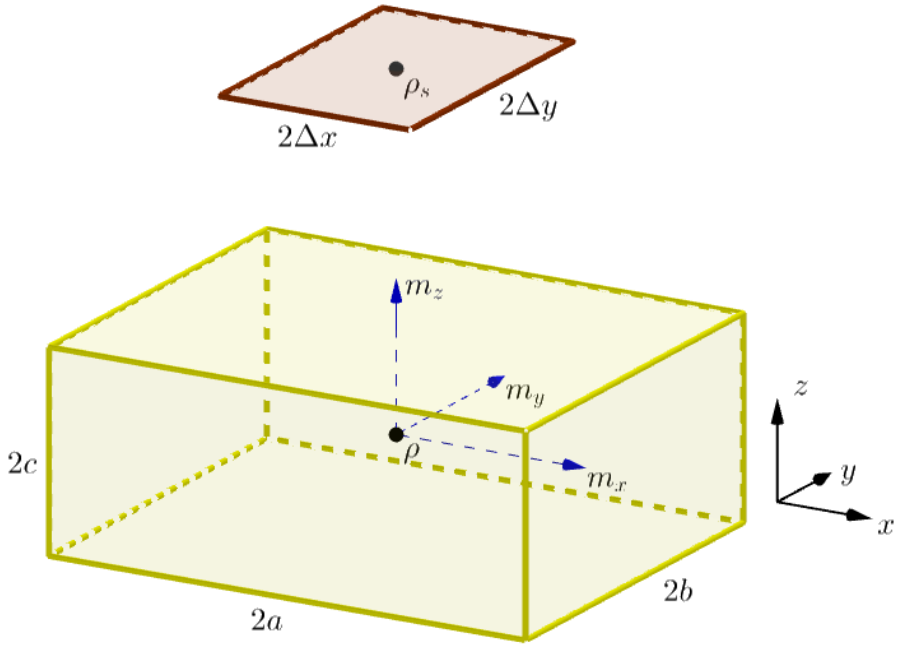

Figure 1: Setting of sensor and cuboid.

Now, let's say we have the vector $(x'', y'', 0)$ originating from the center of the sensor ρ_s. The location it reaches within the sensor is $\boldsymbol{r''} = \begin{pmatrix} x'' + \xi_s \\ y'' + \eta_s \\ \zeta_s \end{pmatrix}$. We have the vector (x', y', z') originating from the center of the cuboid ρ to the point $\boldsymbol{r'} = \begin{pmatrix} x' + \xi \\ y' + \eta \\ z' + \zeta \end{pmatrix}$ on the border of C. The distance between $\boldsymbol{r''}$ and $\boldsymbol{r'}$ is $|\boldsymbol{r''} - \boldsymbol{r'}|$. See figure 2.

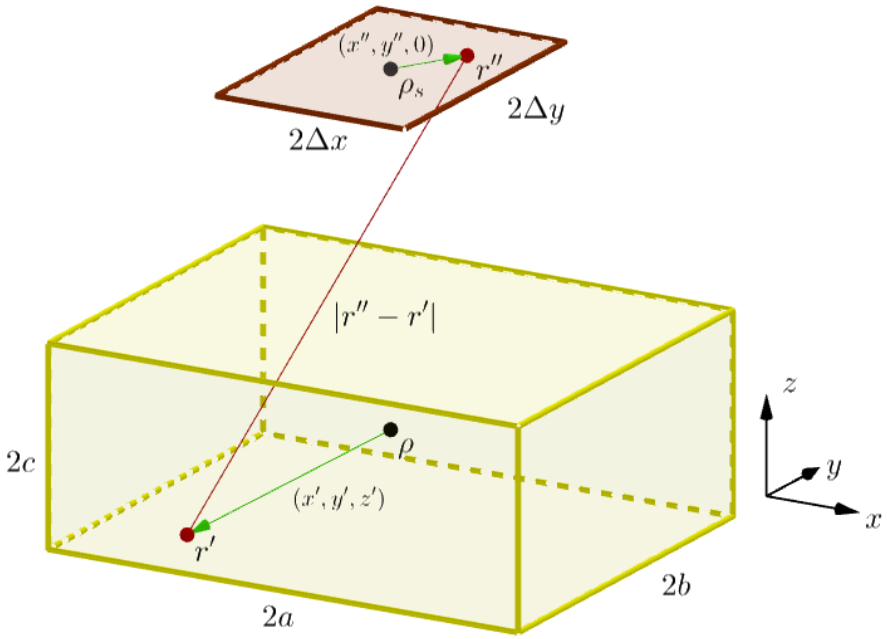

Figure 2: Setting of sensor and cuboid with vectors to $\boldsymbol{r'}$ and $\boldsymbol{r''}$.

The magnetization at any point $\boldsymbol{r'}$ on ∂C creates a magnetic potential $\Phi(\boldsymbol{r''})$ at point $\boldsymbol{r''}$ on the sensor. Looking at the whole border of C (so at all possible locations of $\boldsymbol{r'}$), we get the superposition integral for potential [8]:

$$\Phi(\boldsymbol{r''}) = \frac{1}{4\pi} \int_{\partial C} \frac{\boldsymbol{M} \cdot \boldsymbol{dS'}}{|\boldsymbol{r''} - \boldsymbol{r'}|}.$$

For the magnetic induction at $\boldsymbol{r''}$, we have

$$\boldsymbol{B}(\boldsymbol{r''}) = -\mu_0 \nabla \Phi(\boldsymbol{r''}).$$

Now, in order to find the magnetic flux A measured by the sensor with center ρ_s we need this magnetic induction for all possible locations of $\boldsymbol{r''}$ on the sensor, so for the whole sensor ∂S:

$$\begin{aligned} A(\rho_s) &= \int_{\partial S} \boldsymbol{B}(\boldsymbol{r''}) dx'' dy'' \\ &= \int_{\partial S} -\mu_0 \nabla \Phi(\boldsymbol{r''}) dx'' dy'' \\ &= -\mu_0 \int_{\partial S} \frac{\partial}{\partial z''} \Phi(\boldsymbol{r''}) dx'' dy'' \qquad \text{(sensor measures flux in } z\text{-direction)} \\ &= -\frac{\mu_0}{4\pi} \frac{\partial}{\partial z''} \int_{\partial S} \int_{\partial C} \frac{\boldsymbol{M} \cdot \boldsymbol{dS'}}{|\boldsymbol{r''} - \boldsymbol{r'}|} dx'' dy''. \end{aligned} \tag{1}$$

We have just described how we can find the flux of a magnetic cuboid when we have information on the dimension and location of both the cuboid and the sensor. In the next section, we will look at the situation of multiple magnetic cuboids and thereafter multiple particles.

2.2 Measuring flux of multiple magnetic particles

First, we are going to rewrite formula 1. Let's name two opposite faces of the cuboid in the x-direction X_1 and X_2 (figure 3) and look at face X_1 first. On this face, $x' = a$[1] and for $\boldsymbol{M} \cdot \boldsymbol{dS'}$ of formula 1 we have

[1] You can also choose $x' = -a$ and further on $x' = a$, switching these will not make a difference in the end.

$$\boldsymbol{M}\cdot\boldsymbol{dS'}=\begin{pmatrix}m_x\\m_y\\m_z\end{pmatrix}\cdot\begin{pmatrix}dy'dz'\\0\\0\end{pmatrix}=m_x dy'dz'.$$

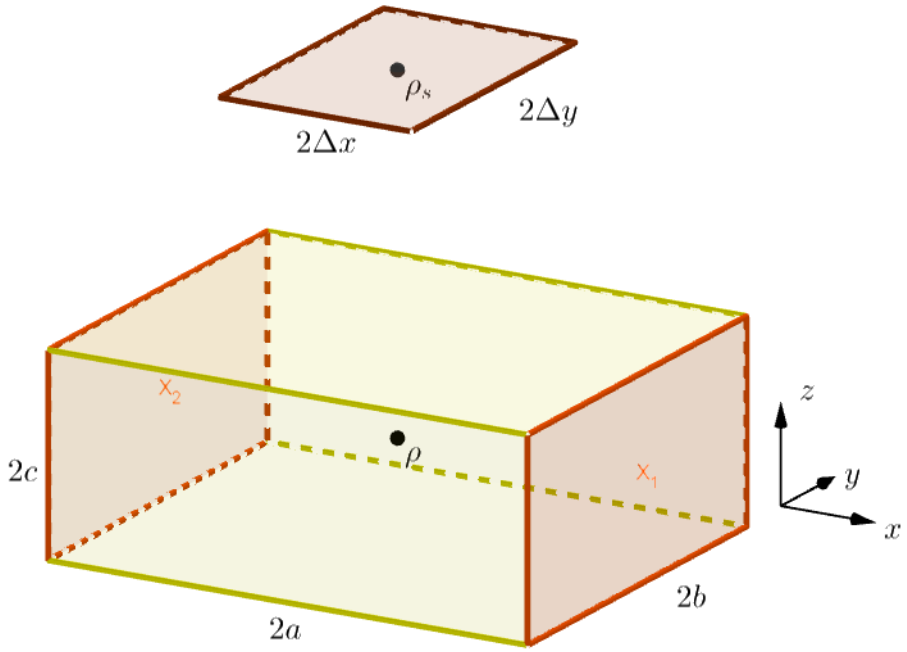

Figure 3: Faces X_1 and X_2 of the cuboid.

Now, for the flux of face X_1 we get

$$A_{X_1}(\rho_s)=-\frac{\mu_0}{4\pi}\frac{\partial}{\partial z''}\int_{\partial S}\int_{\partial C}\frac{m_x}{|\boldsymbol{r''}-\boldsymbol{r'}|_{x'=a}}dy'dz'dx''dy''.$$

For the other face X_2 we have $x'=-a$ and

$$\boldsymbol{M}\cdot\boldsymbol{dS'}=\begin{pmatrix}m_x\\m_y\\m_z\end{pmatrix}\cdot\begin{pmatrix}-dy'dz'\\0\\0\end{pmatrix}=-m_x dy'dz',$$

so for the flux of face X_2 we get

$$A_{X_2}(\rho_s)=-\frac{\mu_0}{4\pi}\frac{\partial}{\partial z''}\int_{\partial S}\int_{\partial C}\frac{-m_x}{|\boldsymbol{r''}-\boldsymbol{r'}|_{x'=-a}}dy'dz'dx''dy''.$$

As we want the total flux, we need to add the fluxes of these faces:

$$\begin{aligned}A_X(\rho_s)&=A_{X_1}(\rho_s)+A_{X_2}(\rho_s)\\&=-\frac{\mu_0}{4\pi}\frac{\partial}{\partial z''}\int_{\partial S}\int_{\partial C}\frac{m_x}{|\boldsymbol{r''}-\boldsymbol{r'}|_{x'=-a}}dy'dz'dx''dy''+-\frac{\mu_0}{4\pi}\frac{\partial}{\partial z''}\int_{\partial S}\int_{\partial C}\frac{-m_x}{|\boldsymbol{r''}-\boldsymbol{r'}|_{x'=-a}}dy'dz'dx''dy''\\&=-\frac{\mu_0 m_x}{4\pi}\frac{\partial}{\partial z''}\left(\int_{\partial S}\int_{\partial C}\frac{1}{|\boldsymbol{r''}-\boldsymbol{r'}|_{x'=a}}dy'dz'dx''dy''-\int_{\partial S}\int_{\partial C}\frac{1}{|\boldsymbol{r''}-\boldsymbol{r'}|_{x'=-a}}dy'dz'dx''dy''\right)\end{aligned}$$

$$
\begin{aligned}
&= -\frac{\mu_0 m_x}{4\pi}\frac{\partial}{\partial z''}\int_{\partial S}\int_{\partial C}\frac{1}{|\boldsymbol{r''}-\boldsymbol{r'}|}dy'dz'dx''dy''\Bigg|_{x'=-a}^{x'=a}\\
&= \left(-\frac{\mu_0}{4\pi}\frac{\partial}{\partial z''}\int_{-\Delta y}^{\Delta y}\int_{-\Delta x}^{\Delta x}\int_{-c}^{c}\int_{-b}^{b}\frac{1}{|\boldsymbol{r''}-\boldsymbol{r'}|}dy'dz'dx''dy''\Bigg|_{x'=-a}^{x'=a}\right)\cdot m_x\\
&= W_X m_x.
\end{aligned}
$$

In the same way, we can find alike formulas when looking at opposite faces in the y-direction and in the z-direction:

$$
\begin{aligned}
A_Y(\rho_s) &= \left(-\frac{\mu_0}{4\pi}\frac{\partial}{\partial z''}\int_{-\Delta y}^{\Delta y}\int_{-\Delta x}^{\Delta x}\int_{-c}^{c}\int_{-a}^{a}\frac{1}{|\boldsymbol{r''}-\boldsymbol{r'}|}dx'dz'dx''dy''\Bigg|_{y'=-b}^{y'=b}\right)\cdot m_y\\
&= W_Y m_y,
\end{aligned}
$$

and

$$
\begin{aligned}
A_Z(\rho_s) &= \left(-\frac{\mu_0}{4\pi}\frac{\partial}{\partial z''}\int_{-\Delta y}^{\Delta y}\int_{-\Delta x}^{\Delta x}\int_{-b}^{b}\int_{-a}^{a}\frac{1}{|\boldsymbol{r''}-\boldsymbol{r'}|}dx'dy'dx''dy''\Bigg|_{z'=-c}^{z'=c}\right)\cdot m_z\\
&= W_Z m_z.
\end{aligned}
$$

Adding the fluxes of the three sets of opposing faces results in the flux of the total border of one cuboid, so formula 1 becomes

$$
\begin{aligned}
A(\rho_s) &= A_X(\rho_s) + A_Y(\rho_s) + A_Z(\rho_s)\\
&= W_X m_x + W_Y m_y + W_Z m_z.
\end{aligned}
$$

Let us now assume that we have K magnetic cuboids. For every cuboid we have different a, b, c, ρ and $\boldsymbol{M}$ and so different W_X, W_Y, W_Z, m_x, m_y and m_z. Now, the total flux measured by the sensor is the sum of the fluxes of all K cuboids:

$$
\begin{aligned}
A(\rho_s) &= \sum_{j=1}^{K}\Big(A_{X_j}(\rho_s) + A_{Y_j}(\rho_s) + A_{Z_j}(\rho_{s_i})\Big)\\
&= \sum_{j=1}^{K}\Big(W_{X_j}m_{x_j} + W_{Y_j}m_{y_j} + W_{Z_j}m_{z_j}\Big)\\
&= \sum_{j=1}^{K}W_{X_j}m_{x_j} + \sum_{j=1}^{K}W_{Y_j}m_{y_j} + \sum_{j=1}^{K}W_{Z_j}m_{z_j}. \qquad (2)
\end{aligned}
$$

The K magnetic cuboids represent the natural situation of K magnetic particles. However, natural magnetic particles are not cuboid-shaped: in a natural sample of magnetic rock we will encounter particles with all different dimensions. For information on these dimensions, tomographic imaging can be used. After determining dimensions and locations, every particle can be partitioned into non-overlapping cuboids (see chapter 4). This means we have cuboids again and so our calculations still hold. Partitioning K magnetic particles in $N \geq K$ cuboids changes formula 2 to

$$
A(\rho_s) = \sum_{j=1}^{N}W_{X_j}m_{x_j} + \sum_{j=1}^{N}W_{Y_j}m_{y_j} + \sum_{j=1}^{N}W_{Z_j}m_{z_j}.
$$

Up until now, we have assumed the scanner used to measure the magnetic flux has one sensor. However, the SQUID scanner used contains a grid of multiple sensors. In the next section, we will look at the total flux of all cuboids measured by all these sensors.

2.3 Inverse model

We have a scanner with a grid of P sensors. For every sensor we have a different ρ_s and so again different W_X, W_Y, W_Z ($\Delta x, \Delta y$ are the same for all sensors). In matrix form, formula 2.2 for the total flux of all N cuboids measured by sensor i with $i = 1, ..., P$ is

$$A(\rho_{s_i}) = \begin{bmatrix} W_{X_{i1}} & \cdots & W_{X_{iN}} \end{bmatrix} \begin{bmatrix} m_{x_1} \\ \vdots \\ m_{x_N} \end{bmatrix} + \begin{bmatrix} W_{Y_{i1}} & \cdots & W_{Y_{iN}} \end{bmatrix} \begin{bmatrix} m_{y_1} \\ \vdots \\ m_{y_N} \end{bmatrix} + \begin{bmatrix} W_{Z_{i1}} & \cdots & W_{Z_{iN}} \end{bmatrix} \begin{bmatrix} m_{z_1} \\ \vdots \\ m_{z_N} \end{bmatrix}.$$

The scanner gives us P measurement results $\phi_i = A(\rho_{s_i})$ and so the output $\boldsymbol{\phi}$ of the scanner is

$$\begin{aligned} \boldsymbol{\phi} = \begin{bmatrix} \phi_1 \\ \vdots \\ \phi_P \end{bmatrix} &= \begin{bmatrix} W_{X_{11}} & \cdots & W_{X_{1N}} \\ \vdots & \ddots & \vdots \\ W_{X_{P1}} & \cdots & W_{X_{PN}} \end{bmatrix} \begin{bmatrix} m_{x_1} \\ \vdots \\ m_{x_N} \end{bmatrix} + \begin{bmatrix} W_{Y_{11}} & \cdots & W_{Y_{1N}} \\ \vdots & \ddots & \vdots \\ W_{Y_{P1}} & \cdots & W_{Y_{PN}} \end{bmatrix} \begin{bmatrix} m_{y_1} \\ \vdots \\ m_{y_N} \end{bmatrix} + \begin{bmatrix} W_{Z_{11}} & \cdots & W_{Z_{1N}} \\ \vdots & \ddots & \vdots \\ W_{Z_{P1}} & \cdots & W_{Z_{PN}} \end{bmatrix} \begin{bmatrix} m_{z_1} \\ \vdots \\ m_{z_N} \end{bmatrix} \\ &= L_X \begin{bmatrix} m_{x_1} \\ \vdots \\ m_{x_N} \end{bmatrix} + L_Y \begin{bmatrix} m_{y_1} \\ \vdots \\ m_{y_N} \end{bmatrix} + L_Z \begin{bmatrix} m_{z_1} \\ \vdots \\ m_{z_N} \end{bmatrix} \\ &= L\boldsymbol{m}_N. \end{aligned}$$

In this model $\boldsymbol{\phi} = L\boldsymbol{m}_N$, every cuboid is treated as a single magnetic item with its own magnetization. However, we have not N but $K \leq N$ different magnetizations, so instead of $\boldsymbol{m}_N$, in the model we want to have

$$\boldsymbol{m} = \begin{bmatrix} m_{x_1} & \cdots & m_{x_K} & m_{y_1} & \cdots & m_{y_K} & m_{z_1} & \cdots & m_{z_K} \end{bmatrix}^T.$$

We can get this by using a $3N \times 3K$-matrix B which multiplied on the right by $\boldsymbol{m}$ gives $\boldsymbol{m}_N$. For example, let's say we have $N = 3$ and $K = 2$ with cuboid 1 and 3 belonging to the same particle:

$$\boldsymbol{m}_N = \begin{bmatrix} m_{x_1} \\ m_{x_2} \\ m_{x_3} \\ m_{y_1} \\ m_{y_2} \\ m_{y_3} \\ m_{z_1} \\ m_{z_2} \\ m_{z_3} \end{bmatrix}, \quad \boldsymbol{m} = \begin{bmatrix} m_{x_1} = m_{x_3} \\ m_{x_2} \\ m_{y_1} = m_{y_3} \\ m_{y_2} \\ m_{z_1} = m_{z_3} \\ m_{z_2} \end{bmatrix} = \begin{bmatrix} \bar{m}_{x_1} \\ \bar{m}_{x_2} \\ \bar{m}_{y_1} \\ \bar{m}_{y_2} \\ \bar{m}_{z_1} \\ \bar{m}_{z_2} \end{bmatrix}.$$

Then, with matrix B we get

$$B\boldsymbol{m} = \begin{bmatrix} 1 & 0 & 0 & 0 & 0 & 0 \\ 0 & 1 & 0 & 0 & 0 & 0 \\ 1 & 0 & 0 & 0 & 0 & 0 \\ 0 & 0 & 1 & 0 & 0 & 0 \\ 0 & 0 & 0 & 1 & 0 & 0 \\ 0 & 0 & 1 & 0 & 0 & 0 \\ 0 & 0 & 0 & 0 & 1 & 0 \\ 0 & 0 & 0 & 0 & 0 & 1 \\ 0 & 0 & 0 & 0 & 1 & 0 \end{bmatrix} \begin{bmatrix} \bar{m}_{x_1} \\ \bar{m}_{x_2} \\ \bar{m}_{y_1} \\ \bar{m}_{y_2} \\ \bar{m}_{z_1} \\ \bar{m}_{z_2} \end{bmatrix} = \begin{bmatrix} m_{x_1} \\ m_{x_2} \\ m_{x_3} \\ m_{y_1} \\ m_{y_2} \\ m_{y_3} \\ m_{z_1} \\ m_{z_2} \\ m_{z_3} \end{bmatrix} = \boldsymbol{m}_N.$$

In general, B contains only elements 1 and 0 to make sure the elements of $\boldsymbol{m}$ are duplicated the right amount of times in the right order to get $\boldsymbol{m}_N$.
Taking $Q = LB$, the model we have becomes

$$\boldsymbol{\phi} = L\boldsymbol{m}_N = LB\boldsymbol{m} = Q\boldsymbol{m},$$

where Q is a $P \times 3K$-matrix consisting of (summands of) $W_{X_{ij}}, W_{Y_{ij}}$ and $W_{Z_{ij}}$ with $i = 1, ..., P$ and $j = 1, ..., N$.

We have now found a way to express the flux measurements $\boldsymbol{\phi}$ in two components Q and $\boldsymbol{m}$, of which the latter contains the desired magnetization per particle. In this model $\boldsymbol{\phi} = Q\boldsymbol{m}$, the elements of the $P \times 3K$-matrix Q are linear [2], so what we have now is a linear inverse problem. In the next chapter, we will elaborate on this and how $\boldsymbol{m}$ can be determined.

[2] For elaboration on the elements of Q, please refer to the supporting materials of de Groot et al. (2018).

3 Inverse problem

In the previous chapter, we have found the model $\boldsymbol{\phi} = Q\boldsymbol{m}$, from which we want to find $\boldsymbol{m}$. If we knew Q was invertible, this would be easily done. However, the chances are high that it is not ($P \gg 3K$, see chapter 5), so we need to find another way to determine $\boldsymbol{m}$. This is an inverse problem, which according to Hadamard (1902 and 1932) is well-posed when a solution exists, this solution is unique and when change in the initial conditions results in change of equal proportion in the solution. In this chapter, we will focus on general inverse theory before applying it to our model in section 3.3. For the first two conditions of Hadamard, we introduce Singular Value Decomposition in section 3.1. With this SVD, we then find out in section 3.2 whether and when these conditions are met for an inverse problem and we discover a pseudo-inverse, which gives us a solution for this problem. In section 3.3, we explore another method to find a solution, which we show is a special case of the pseudo-inverse. We apply this to our model from chapter 2. The third condition of Hadamard will be examined in section 3.4, where we introduce the condition number to examine the stability and thus reliability of our model. When there is a measurement error which is normally distributed, we find a covariance matrix of the inversion result. This matrix allows us to assess the relationships between the vector-components of the magnetizations of all magnetic particles. For both the condition number and covariance matrix, we show examples of possible situations which are modeled with Matlab.

This chapter is largely based on chapter 4 and chapter 6 of the book *A First Course in Numerical Methods* by U.M.Ascher and C.Greif (2011).

3.1 Singular Value Decomposition

Any $m \times n$ matrix M can be decomposed as follows:

$$M = U\Sigma V^T,$$

where U, Σ and V are specific matrices. This is called the Singular Value Decomposition, or the SVD.

Σ is an $m \times n$ matrix which consists of the singular values $\sigma_1 \geq \sigma_2 \geq \cdots \geq \sigma_r > 0$ on (the first part of) its main diagonal, with all other elements being zero:

$$\Sigma = \begin{pmatrix} \sigma_1 & & & & \\ & \sigma_2 & & & \\ & & \ddots & & \\ & & & \sigma_r & \\ & & & & \end{pmatrix}.$$

The singular values σ_i with $i = 0, ..., r$ of M are the square roots of the eigenvalues λ_i of M^TM. r satisfies $r = \text{rank}(M) \leq \min(m, n)$.
V is an orthogonal $n \times n$ matrix whose columns are the eigenvectors of M^TM, and U is an orthogonal $m \times m$ matrix whose columns are the eigenvectors of MM^T. This can be seen by using the SVD of M:

$$\begin{aligned} M^TM &= (U\Sigma V^T)^T U\Sigma V^T & MM^T &= U\Sigma V^T (U\Sigma V^T)^T \\ &= V\Sigma^T U^T U\Sigma V^T & &= U\Sigma V^T V\Sigma^T U^T \\ &= V\Sigma^T\Sigma V^T & &= U\Sigma\Sigma^T U^T, \qquad \text{(orthogonality of } U \text{ and } V\text{)} \end{aligned}$$

so

$$\begin{aligned} M^TMV &= V\Sigma^T\Sigma V^T V & MM^TU &= U\Sigma\Sigma^T U^T U \\ &= V\Sigma^T\Sigma & &= U\Sigma\Sigma^T. \qquad \text{(orthogonality of } U \text{ and } V\text{)} \end{aligned}$$

What we have now are two eigenvalue problems and so the columns of V and U are the eigenvectors of $M^T M$ and MM^T, respectively.

A visualization of the SVD looks as follows:

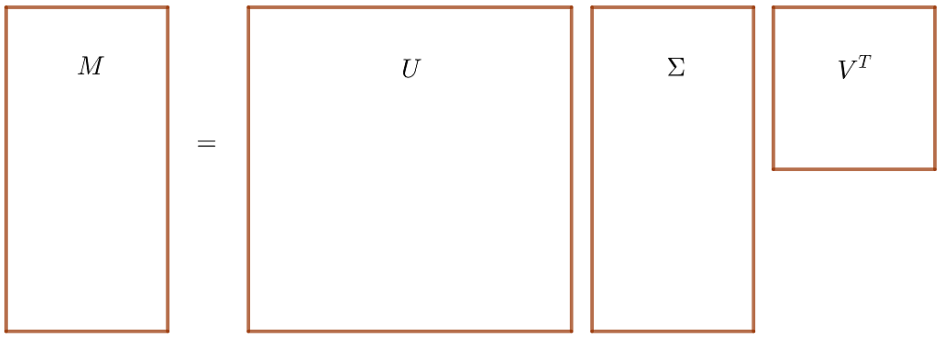

Bear in mind that although in this visualization it looks like $m > n$, this does not need to be the case. While this is where the theory of U.M.Ascher and C.Greif (2011) ends, we would like to simplify the SVD. We know that Σ has $m - r$ rows and $n - r$ columns which contain only zeros. This means that when U is multiplied by Σ, we get an $m \times n$ matrix whose last $n - r$ columns contain only zeros:

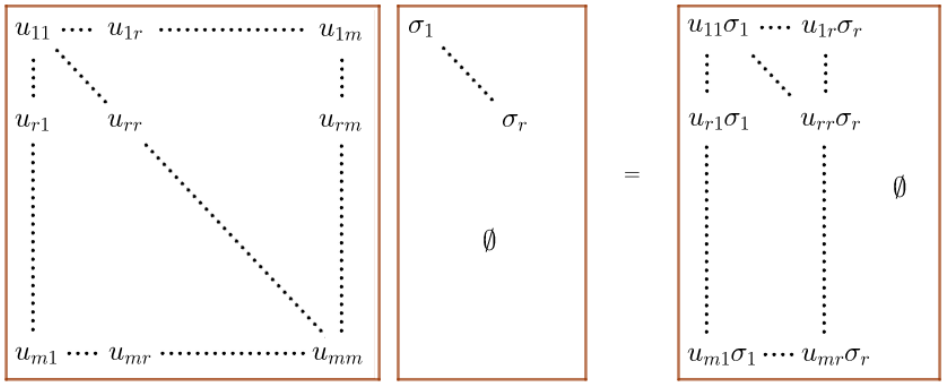

When this resulting matrix is then multiplied by V, we get an $m \times n$ matrix which by the definition of the SVD equals M:

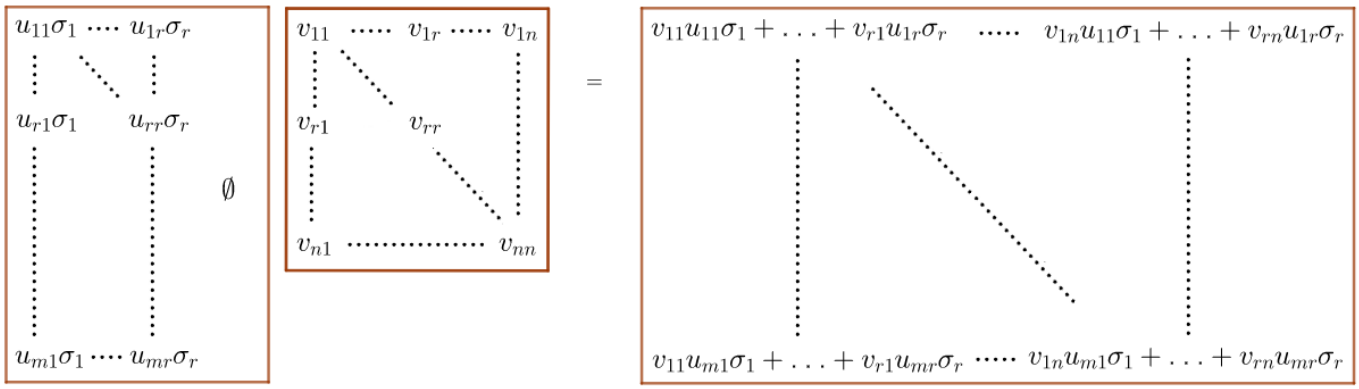

As can be seen, the elements of the last $m - r$ columns of U do not occur in M. The same goes for the elements of the last $n - r$ rows of V^T. We can take these columns and rows out of U and V^T respectively, which results in a simplified SVD

$$M = U_r \Sigma_r V_r^T,$$

in which U_r is the $m \times r$ matrix consisting of the first r columns of U, Σ_r is the $r \times r$ matrix with the singular values on its main diagonal and V_r^T is the $r \times n$ matrix consisting of the first r rows of V^T:

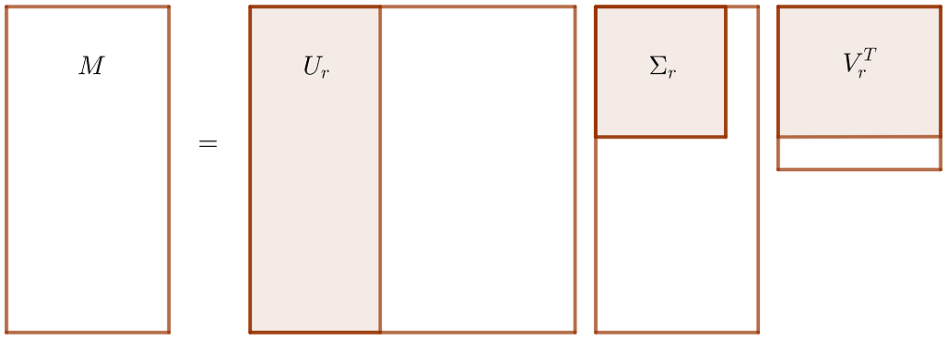

As Σ as opposed to Σ_r can not be inverted (unless $\Sigma = \Sigma_r$), it comes in handy to use this simplified version of the SVD later on.

3.2 Pseudo-inverse

We consider the linear system of equations $A\boldsymbol{x} = \boldsymbol{b}$ with $A \in \mathbb{R}^{m \times n}, \boldsymbol{x} \in \mathbb{R}^n$ and $\boldsymbol{b} \in \mathbb{R}^m$ for which we want to find $\boldsymbol{x}$. The first two conditions of Hadamard for this inverse problem are that a solution needs to exist and this solution needs to be unique. We examine both conditions in this section.

First, we want to know whether a solution exists.
When we assume we can not find an $\boldsymbol{x}$ which satisfies $A\boldsymbol{x} = \boldsymbol{b}$, this means that $\boldsymbol{b}$ is not in the range of A. We then want to find a solution for $A\boldsymbol{x} = \tilde{\boldsymbol{b}}$ with $\tilde{\boldsymbol{b}} \in \text{range}(A)$ as close to $\boldsymbol{b}$ as possible, to optimally approximate the desired solution $\boldsymbol{x}$. We use the orthogonal projection of $\boldsymbol{b}$ onto the range of A for this. From the previous section we know U_r is the orthonormal basis of range(A), so we get [6]

$$\tilde{\boldsymbol{b}} = U_r U_r^T \boldsymbol{b} = A\boldsymbol{x}.$$

We know that we can decompose A to $A = U_r \Sigma_r V_r^T$ with Singular Value Decomposition, which now gives us

$$\begin{aligned} A\boldsymbol{x} &= U_r U_r^T \boldsymbol{b} \\ U_r \Sigma_r V_r^T \boldsymbol{x} &= U_r U_r^T \boldsymbol{b} \\ \Sigma_r V_r^T \boldsymbol{x} &= U_r^T \boldsymbol{b} \\ V_r^T \boldsymbol{x} &= \Sigma_r^{-1} U_r^T \boldsymbol{b}. \end{aligned} \tag{3}$$

This system of equations guarantees solutions for $\boldsymbol{x}$, satisfying the first condition of Hadamard.

We now want to find such a solution and determine whether it is unique.

When $V_r V_r^T = I$, we find

$$\begin{aligned} V_r V_r^T \boldsymbol{x} &= V_r \Sigma_r^{-1} U_r^T \boldsymbol{b} \\ \boldsymbol{x} &= V_r \Sigma_r^{-1} U_r^T \boldsymbol{b}. \end{aligned}$$

When $V_r V_r^T \neq I$, we can not do this and need to find another way to find a solution.
As V_r is an (orthonormal) basis in a subspace of $\mathbb{R}^n$, $V_r \tilde{\boldsymbol{x}}$ is in that subspace for any $\tilde{\boldsymbol{x}} \in \mathbb{R}^r$. As $(I - V_r V_r^T)\boldsymbol{y}$ is in the orthogonal complement of that subspace for any $\boldsymbol{y} \in \mathbb{R}^n$, a solution $\boldsymbol{x} \in \mathbb{R}^n$ can be written as [6]

$$\boldsymbol{x} = V_r\tilde{\boldsymbol{x}} + (I - V_rV_r^T)\boldsymbol{y}. \tag{4}$$

As $\boldsymbol{y}$ can be chosen arbitrarily, it makes sense to choose $\boldsymbol{y} = \boldsymbol{0}$ for sake of simplicity, which leaves us with $\boldsymbol{x} = V_r\tilde{\boldsymbol{x}}$. We then have

$$\Sigma_r^{-1}U^T\boldsymbol{b} = V_r^T\boldsymbol{x} = V_r^TV_r\tilde{\boldsymbol{x}} = \tilde{\boldsymbol{x}}. \qquad \text{(recall equation 3)}$$

Combining this with equation 4 (with $\boldsymbol{y} = \boldsymbol{0}$), we get

$$\boldsymbol{x} = V_r\Sigma_r^{-1}U^T\boldsymbol{b}, \tag{5}$$

which is the same solution as when $V_rV_r^T = I$.

According to R. Penrose (1955), for every matrix A there exists a unique generalized inverse $A^\dagger$. We call this the pseudo-inverse. We found this pseudo-inverse for any matrix A:

$$A^\dagger = V_r\Sigma_r^{-1}U_r^T.$$

It follows that solution 5 is the unique solution for $A\boldsymbol{x} = \boldsymbol{b}$.

The first two conditions of Hadamard are now met: a solution for the problem exists and this solution is unique. The unique solution can also be found using Least Squares Approximation, which we explore in the next section.

3.3 Least squares problem

Again, we consider the linear system of equations $A\boldsymbol{x} = \boldsymbol{b}$ with $A \in \mathbb{R}^{m\times n}, \boldsymbol{x} \in \mathbb{R}^n$ and $\boldsymbol{b} \in \mathbb{R}^m$ for which we want to find $\boldsymbol{x}$. If we knew A was invertible, we could easily multiply both the left and right side of the model by A^{-1} to get the solution $\boldsymbol{x} = A^{-1}\boldsymbol{b}$. Unfortunately, we do not know whether the inverse exists. We are going to determine the best possible solution or the best-fitting $\boldsymbol{x}$ for this model. This is done by finding the minimal difference between $A\boldsymbol{x}$ and $\boldsymbol{b}$, or

$$\min_{\boldsymbol{x}} ||\boldsymbol{b} - A\boldsymbol{x}||_2.$$

This is called the least squares problem. We rewrite this to

$$\min_{\boldsymbol{x}} \frac{1}{2}||\boldsymbol{b} - A\boldsymbol{x}||_2^2 = \min_{\boldsymbol{x}} \Psi(\boldsymbol{x}).$$

Squaring the norm and dividing it by 2 will yield the same solution, rewriting the least squares problem as such will be more convenient as will be pointed out later on.
We have

$$\begin{aligned}\Psi(\boldsymbol{x}) &= \frac{1}{2}||\boldsymbol{b} - A\boldsymbol{x}||_2^2 \\ &= \frac{1}{2}\Big[(b_1 - (a_{1,1}x_1 + ... + a_{1,n}x_n))^2 + (b_2 - (a_{2,1}x_1 + ... + a_{2,n}x_n))^2 + ... + (b_m - (a_{m,1}x_1 + ... + a_{m,n}x_n))^2\Big] \\ &= \frac{1}{2}\sum_{i=1}^{m}\Big(b_i - \sum_{j=1}^{n}a_{i,j}x_j\Big)^2.\end{aligned}$$

We want to find the minimum of this function, so we want the solutions for $\nabla\Psi(\boldsymbol{x}) = \boldsymbol{0}$, or equivalently $\frac{\partial}{\partial x_k}\Psi(\boldsymbol{x}) = 0$ for $k = 1, ..., n$. We get (now it comes in handy that we rewrote the least squares problem):

$$\frac{\partial}{\partial x_k}\Psi(\boldsymbol{x}) = \frac{\partial}{\partial x_k}\left[\frac{1}{2}\sum_{i=1}^{m}\Big(b_i - \sum_{j=1}^{n}a_{i,j}x_j\Big)^2\right] \qquad \text{(for } k = 1, ..., n\text{)}$$

$$= \sum_{i=1}^{m} \Big[\Big(b_i - \sum_{j=1}^{n} a_{i,j} x_j \Big) (-a_{i,k}) \Big] \qquad (\text{for } k = 1, ..., n)$$

$$= \sum_{i=1}^{m} \Big(- a_{i,k} b_i + a_{i,k} \sum_{j=1}^{n} a_{i,j} x_j \Big) \qquad (\text{for } k = 1, ..., n)$$

$$= - \sum_{i=1}^{m} a_{i,k} b_i + \sum_{i=1}^{m} \Big(a_{i,k} \sum_{j=1}^{n} a_{i,j} x_j \Big) = 0. \qquad (\text{for } k = 1, ..., n)$$

So,

$$\sum_{i=1}^{m} a_{i,k} b_i = \sum_{i=1}^{m} \Big(a_{i,k} \sum_{j=1}^{n} a_{i,j} x_j \Big), \qquad (\text{for } k = 1, ..., n)$$

which is in fact

$$A^T \boldsymbol{b} = A^T A \boldsymbol{x}. \tag{6}$$

To see this more clearly, consider

$$\sum_{i=1}^{m} a_{i,k} b_i = a_{1,k} b_1 + ... + a_{m,k} b_m \qquad (\text{for } k = 1, ..., n)$$

$$= \begin{bmatrix} a_{1k} & \cdots & a_{mk} \end{bmatrix} \begin{bmatrix} b_1 \\ \vdots \\ b_m \end{bmatrix} \qquad (\text{for } k = 1, ..., n)$$

$$= \begin{bmatrix} a_{11} & \cdots & a_{m1} \\ \vdots & \ddots & \vdots \\ a_{1n} & \cdots & a_{mn} \end{bmatrix} \begin{bmatrix} b_1 \\ \vdots \\ b_m \end{bmatrix}$$

$$= A^T \boldsymbol{b},$$

and

$$\sum_{i=1}^{m} \Big(a_{i,k} \sum_{j=1}^{n} a_{i,j} x_j \Big) = \sum_{i=1}^{m} \Big(a_{i,k} (a_{i,1} x_1 + ... + a_{i,n} x_n) \Big) \qquad (\text{for } k = 1, ..., n)$$

$$= \sum_{i=1}^{m} \Big(a_{i,k} \begin{bmatrix} a_{i1} & \cdots & a_{in} \end{bmatrix} \begin{bmatrix} x_1 \\ \vdots \\ x_n \end{bmatrix} \Big) \qquad (\text{for } k = 1, ..., n)$$

$$= \Big(a_{1,k} \begin{bmatrix} a_{11} & \cdots & a_{1n} \end{bmatrix} + ... + a_{m,k} \begin{bmatrix} a_{m1} & \cdots & a_{mn} \end{bmatrix} \Big) \begin{bmatrix} x_1 \\ \vdots \\ x_n \end{bmatrix} \qquad (\text{for } k = 1, ..., n)$$

$$= \Big(\begin{bmatrix} a_{1k} a_{11} & \cdots & a_{1k} a_{1n} \end{bmatrix} + ... + \begin{bmatrix} a_{mk} a_{m1} & \cdots & a_{mk} a_{mn} \end{bmatrix} \Big) \begin{bmatrix} x_1 \\ \vdots \\ x_n \end{bmatrix} \qquad (\text{for } k = 1, ..., n)$$

$$= \begin{bmatrix} a_{1k} a_{11} + ... + a_{mk} a_{m1} & \cdots & a_{1k} a_{1n} + ... + a_{mk} a_{mn} \end{bmatrix} \begin{bmatrix} x_1 \\ \vdots \\ x_n \end{bmatrix} \qquad (\text{for } k = 1, ..., n)$$

$$
\begin{aligned}
&= \begin{bmatrix} a_{1k} & \cdots & a_{mk} \end{bmatrix} \begin{bmatrix} a_{11} & \cdots & a_{1n} \\ \vdots & \ddots & \vdots \\ a_{m1} & \cdots & a_{mn} \end{bmatrix} \begin{bmatrix} x_1 \\ \vdots \\ x_n \end{bmatrix} && \text{(for } k = 1, ..., n\text{)} \\
&= \begin{bmatrix} a_{11} & \cdots & a_{m1} \\ \vdots & \ddots & \vdots \\ a_{1n} & \cdots & a_{mn} \end{bmatrix} \begin{bmatrix} a_{11} & \cdots & a_{1n} \\ \vdots & \ddots & \vdots \\ a_{m1} & \cdots & a_{mn} \end{bmatrix} \begin{bmatrix} x_1 \\ \vdots \\ x_n \end{bmatrix} \\
&= A^T A\boldsymbol{x}.
\end{aligned}
$$

When $\text{rank}(A) = n$ with $m \geq n$ (in other words A has full column rank), the $n \times n$ matrix $A^T A$ has full column rank and so is invertible. Both sides of equation 6 can be multiplied on the left by $(A^T A)^{-1}$, yielding the solution

$$(A^T A)^{-1} A^T \boldsymbol{b} = \boldsymbol{x}. \tag{7}$$

In the previous section, we found the unique solution $\boldsymbol{x} = A^\dagger \boldsymbol{b} = V_r \Sigma_r^{-1} U_r^T \boldsymbol{b}$, which then must be the same as solution 7:

$$
\begin{aligned}
\boldsymbol{x} &= (A^T A)^{-1} A^T \boldsymbol{b} \\
&= \left[(U_r \Sigma_r {V_r}^T)^T (U_r \Sigma_r {V_r}^T) \right]^{-1} (U_r \Sigma_r {V_r}^T)^T \boldsymbol{b} \\
&= \left[V_r {\Sigma_r}^T {U_r}^T U_r \Sigma_r {V_r}^T \right]^{-1} V_r {\Sigma_r}^T {U_r}^T \boldsymbol{b} \\
&= (V_r {\Sigma_r}^T \Sigma_r {V_r}^T)^{-1} V_r {\Sigma_r}^T {U_r}^T \boldsymbol{b} && \text{(orthogonality of U)} \\
&= ({V_r}^T)^{-1} {\Sigma_r}^{-1} ({\Sigma_r}^T)^{-1} {V_r}^{-1} V_r {\Sigma_r}^T {U_r}^T \boldsymbol{b} \\
&= V_r {\Sigma_r}^{-1} ({\Sigma_r}^T)^{-1} {\Sigma_r}^T {U_r}^T \boldsymbol{b} && \text{(orthogonality of V)} \\
&= V_r {\Sigma_r}^{-1} {U_r}^T \boldsymbol{b} \\
&= A^\dagger \boldsymbol{b}.
\end{aligned}
$$

The Least Squares solution is a special case of the pseudo-inverse: it is only the solution when the linear operator A in the linear system $A\boldsymbol{x} = \boldsymbol{b}$ has full column rank.

Returning to the model we are interested in, $\boldsymbol{\phi} = Q\boldsymbol{m}$ with $\boldsymbol{\phi} \in \mathbb{R}^P, Q \in \mathbb{R}^{P \times 3K}$ and $\boldsymbol{m} \in \mathbb{R}^{3K}$, we now know that we can use the pseudo-inverse of Q to find $\boldsymbol{m} = Q^\dagger \boldsymbol{\phi} = V_r {\Sigma_r}^{-1} {U_r}^T \boldsymbol{\phi}$. However, we assume Q has full column rank [3], which means we can use the Least Squares solution to find $\boldsymbol{m} = Q^\dagger \boldsymbol{\phi} = (Q^T Q)^{-1} Q^T \boldsymbol{\phi}$.

In the next section we will look at the stability of our model to review the last condition of Hadamard.

3.4 Reliability

The last condition of Hadamard states that the solution of an inverse problem changes proportionally to changes in the initial conditions. This section, we will discuss the condition number which expresses this sensitivity. We also look at the covariance matrix in order to review the margin of error on the solution.

3.4.1 Condition number

In chapter 2 we have found the model $\boldsymbol{\phi} = Q\boldsymbol{m}$, with which we can find $\boldsymbol{m} = Q^\dagger \boldsymbol{\phi}$. However, there will be some sort of noise $\boldsymbol{\epsilon} = (\epsilon_1, ..., \epsilon_P)$ from the scanner used to measure $\boldsymbol{\phi}$, so in reality we have $Q\boldsymbol{m}_\epsilon = \boldsymbol{\phi} + \boldsymbol{\epsilon}$, yielding $\boldsymbol{m}_\epsilon = Q^\dagger(\boldsymbol{\phi} + \boldsymbol{\epsilon})$. We assume $||\boldsymbol{\epsilon}||$ is bounded, where with $|| \cdot ||$ (and any norm hereafter) we mean the 2-norm.

[3] For elaboration, please refer to chapter 5

For the difference between the optimal magnetization $\boldsymbol{m} = \boldsymbol{m}_0$ and the magnetization with error $\boldsymbol{m}_\epsilon$ we get

$$\begin{aligned} ||\boldsymbol{m}_\epsilon - \boldsymbol{m}_0|| &= ||Q^\dagger(\boldsymbol{\phi} + \boldsymbol{\epsilon}) - Q^\dagger\boldsymbol{\phi}|| \\ &= ||Q^\dagger\boldsymbol{\epsilon}|| \\ &\leq ||Q^\dagger||\ ||\boldsymbol{\epsilon}||. \end{aligned} \tag{8}$$

With the ratio $\delta = \frac{||(\boldsymbol{\phi}+\boldsymbol{\epsilon})-\boldsymbol{\phi}||}{||\boldsymbol{\phi}||} = \frac{||\boldsymbol{\epsilon}||}{||\boldsymbol{\phi}||}$, we have

$$\begin{aligned} ||\boldsymbol{\epsilon}|| &= ||\boldsymbol{\phi}||\delta \\ &= ||Q\boldsymbol{m}_0||\delta \\ &\leq ||Q||\ ||\boldsymbol{m}_0||\delta, \end{aligned} \tag{9}$$

and so, combing inequalities 8 and 9 we find

$$||\boldsymbol{m}_\epsilon - \boldsymbol{m}_0|| \leq ||Q^\dagger||\ ||Q||\ ||\boldsymbol{m}_0||\delta.$$

As the spectral norm of Q and $Q^\dagger$ is their largest singular value , we get $||Q|| = \sigma_1$ and $||Q^\dagger|| = \frac{1}{\sigma_r}$ (see chapter 2) so

$$||\boldsymbol{m}_\epsilon - \boldsymbol{m}_0|| \leq \frac{\sigma_1}{\sigma_r}||\boldsymbol{m}_0||\delta,$$

which gives us

$$\frac{||\boldsymbol{m}_\epsilon - \boldsymbol{m}_0||}{||\boldsymbol{m}_0||} \leq \frac{\sigma_1}{\sigma_r}\frac{||\boldsymbol{\epsilon}||}{||\boldsymbol{\phi}||}. \tag{10}$$

$\frac{\sigma_1}{\sigma_r}$ is called the condition number of Q. Thus, formula 10 tells us that a small condition number means the solution is not very sensitive to changes in the initial conditions (due to noise), whereas a large condition number means high sensitivity. As $\sigma_1 > ... > \sigma_r$, we have $\frac{\sigma_1}{\sigma_r} \geq 1$, so a condition number as close to 1 as possible is ideal.

By determining the condition number, the extent to which the third condition of Hadamard on stability of the solution is met can be found. With a model in Matlab by T. van Leeuwen (appendix A), we look at the condition number with a simple example.

We model two cuboids A and B of equal size ($5 \times 5 \times 5$ µm) and a grid of 50×50 sensors with sides measuring 0.5 µm. The middle points of the cuboids are located at (-5,0,8) and (5,0,8) respectively. Note that these coordinates are based on the sensor grid and not on µm. We assign the cuboids magnetizations $\boldsymbol{m}_1 = (1, 3, -2.6)$ and $\boldsymbol{m}_2 = (-2, -1.8, 4)$ respectively. The total magnetization vector is therefore $\boldsymbol{m} = (1, 3, -2.6, -2, -1.8, 4)$. The cuboids are positioned directly next to each other, see figure 4.

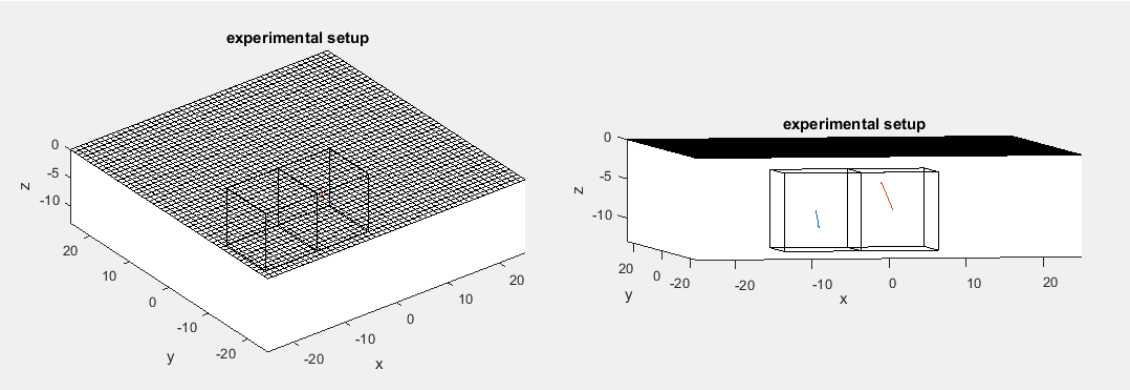

Figure 4: Cuboid A (at (-5,0,8)) and B (at (5,0,8)) with magnetization vectors and sensor grid modeled with Matlab. The left and right image give different views of the same setup.

We move the cuboids apart in the x-direction and let Matlab generate the condition number. The results are in figure 5. As can be seen, the condition number is largest when the cuboids are located directly next to each other. Moving the cuboids apart first results in a lower condition number, but as the distance grows bigger than 15 µm (30 steps of 0.5 µm) the condition number starts increasing again. A reason for this may be that the cuboids are getting too close to the outer edges of the sensor grid. In figure 5, it can be seen clearly that the closer the cuboids get to each other, the greater the increase of the condition number. For the y-direction we get these exact same results, as the movement is the same relative to the sensor grid. It seems that in this case, having a distance of 15 µm in either the x- or y-direction between the magnetized cuboids results in the least sensitive solution.

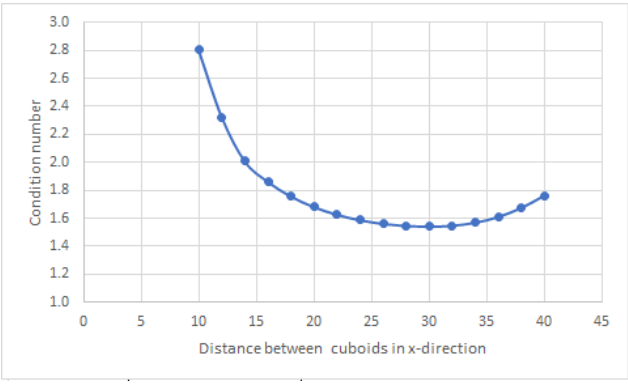

Figure 5: Condition number put against distance between the x-coordinates of the middle points of cuboids A and B. The distance is expressed in grid steps of 0.5 µm.

We now place the cuboids on top of each other at (5,0,10) and (5,0,20) respectively and move them apart in the z-direction. The depth of the model (figure 4) increases automatically when cuboids are located at greater depth. We find condition numbers unlike the ones when moving in the x- and y-direction (figure 6). These condition numbers are high and only increase when the cuboids are being moved apart. This suggests that cuboids overlapping in the z-direction will give a more sensitive solution than when cuboids only overlap in the x- and y-direction.

Distance between cuboids in z-direction	Condition number
10	11.277
12	12.877
14	15.637
16	19.982
18	26.958

Figure 6: Condition number for cuboids which have the same x, y-coordinates but move apart in the z-direction. The distance is expressed in grid steps of 0.5 µm.

3.4.2 Covariance matrix

In the previous section, we assumed that we have an error $\boldsymbol{\epsilon}$ caused by noise in our results: $\boldsymbol{\phi} = Q\boldsymbol{m} + \boldsymbol{\epsilon}$, where $\boldsymbol{\epsilon}$ can be any vector in $\mathbb{R}^P$ with bounded 2-norm. Now, we explore the model when assuming that the elements of the error are normally distributed, or $\epsilon_i \sim N(0, \sigma^2)$ for every $i = 1, ..., P$. This means we have $\mathbb{E}[\epsilon_i] = 0$ and $\mathbb{E}[\epsilon_i^2] = \sigma^2$. As ϵ_i and ϵ_j with $i, j = 1, ..., P$ and $i \neq j$ are independent random variables, we get

$$\mathrm{Cov}(\epsilon_i, \epsilon_j) = \mathbb{E}[(\epsilon_i - \mathbb{E}[\epsilon_i])(\epsilon_j - \mathbb{E}[\epsilon_j])] = \mathbb{E}[\epsilon_i \epsilon_j] = 0.$$

When we have

$$\mathbb{E}[\boldsymbol{\epsilon}\boldsymbol{\epsilon}^T] = \Sigma = \begin{bmatrix} \mathrm{Cov}(\epsilon_1, \epsilon_1) & \dots & \mathrm{Cov}(\epsilon_1, \epsilon_P) \\ \vdots & \ddots & \vdots \\ \mathrm{Cov}(\epsilon_P, \epsilon_1) & \dots & \mathrm{Cov}(\epsilon_P, \epsilon_P) \end{bmatrix} = \begin{bmatrix} \mathbb{E}[\epsilon_1^2] & & \emptyset \\ & \ddots & \\ \emptyset & & \mathbb{E}[\epsilon_P^2] \end{bmatrix} = \begin{bmatrix} \sigma^2 & & \emptyset \\ & \ddots & \\ \emptyset & & \sigma^2 \end{bmatrix} = \sigma^2 I_P,$$

we say $\boldsymbol{\epsilon} \sim N(\mathbf{0}, \Sigma)$, or the error $\boldsymbol{\epsilon}$ is multivariate normally distributed with Σ being the covariance matrix of $\boldsymbol{\epsilon}$ [13].

We have noise-contaminated measurements $\boldsymbol{\phi} = Q\boldsymbol{m} + \boldsymbol{\epsilon}$, so for our by inversion generated magnetization $\hat{\boldsymbol{m}}$ we have

$$\begin{aligned} \hat{\boldsymbol{m}} &= Q^\dagger \boldsymbol{\phi} \\ &= Q^\dagger (Q\boldsymbol{m} + \boldsymbol{\epsilon}) \\ &= Q^\dagger Q \boldsymbol{m} + Q^\dagger \boldsymbol{\epsilon} \\ &= \boldsymbol{m} + Q^\dagger \boldsymbol{\epsilon}. \end{aligned}$$

For the variance of $\hat{\boldsymbol{m}}$, we now find

$$\begin{aligned} \mathrm{Var}(\hat{\boldsymbol{m}}) &= \mathbb{E}\left[(\hat{\boldsymbol{m}} - \boldsymbol{m})(\hat{\boldsymbol{m}} - \boldsymbol{m})^T\right] \\ &= \mathbb{E}\left[(Q^\dagger \boldsymbol{\epsilon})(Q^\dagger \boldsymbol{\epsilon})^T\right] \\ &= \mathbb{E}[Q^\dagger \boldsymbol{\epsilon}\boldsymbol{\epsilon}^T (Q^\dagger)^T] \\ &= Q^\dagger \mathbb{E}[\boldsymbol{\epsilon}\boldsymbol{\epsilon}^T] \left((Q^T Q)^{-1} Q^T\right)^T \\ &= Q^\dagger \sigma^2 I_P Q (Q^T Q)^{-1} \\ &= \sigma^2 (Q^T Q)^{-1}. \qquad (Q^\dagger Q = V_r \Sigma_r^{-1} U_r^T U_r \Sigma_r V_r^T = I) \end{aligned}$$

Recall that we assume Q has full column rank (section 3.3), which is why the inverse $(Q^T Q)^{-1}$ exists. This solution is the covariance matrix of $\hat{\boldsymbol{m}}$ [13]:

$$\sigma^2(Q^TQ)^{-1} = \begin{bmatrix} \mathrm{Cov}(\hat{m}_1,\hat{m}_1) & \cdots & \mathrm{Cov}(\hat{m}_1,\hat{m}_{3K}) \\ \vdots & \ddots & \vdots \\ \mathrm{Cov}(\hat{m}_{3K},\hat{m}_1) & \cdots & \mathrm{Cov}(\hat{m}_{3K},\hat{m}_{3K}) \end{bmatrix}$$
$$= \begin{bmatrix} \mathrm{Var}(\hat{m}_1) & \cdots & \mathrm{Cov}(\hat{m}_1,\hat{m}_{3K}) \\ \vdots & \ddots & \vdots \\ \mathrm{Cov}(\hat{m}_{3K},\hat{m}_1) & \cdots & \mathrm{Var}(\hat{m}_{3K}) \end{bmatrix}.$$

The matrix is symmetric, as $\mathrm{Cov}(\hat{m}_i,\hat{m}_j)$=$\mathrm{Cov}(\hat{m}_j,\hat{m}_i)$. The values represent a certain degree of association between the elements of $\hat{\boldsymbol{m}}$. In order to understand what these values actually mean, we look at the correlation coefficient ρ [13]:

$$\rho_{ij} = \frac{\mathrm{Cov}(\hat{m}_i,\hat{m}_j)}{\sqrt{\mathrm{Var}(\hat{m}_i)\mathrm{Var}(\hat{m}_j)}},$$

where $i,j = 1,...,3K$ and $-1 \leq \rho \leq 1$. A negative correlation means that when $\hat{m}_i$ increases in value, $\hat{m}_j$ decreases. A positive correlation means that when $\hat{m}_i$ increases, $\hat{m}_j$ increases as well. The closer ρ is to 0, the weaker the relationship between $\hat{m}_i$ and $\hat{m}_j$ [10]. See figure 7.

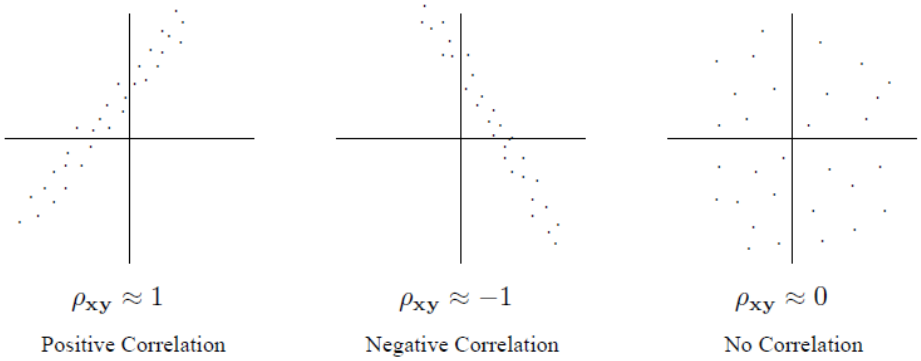

Figure 7: Illustration of the correlation coefficient [10].

When determining magnetizations of particles, we want these magnetizations to be as independent as possible from each other. Then, when one particle is somehow sensitive to magnetic changes in the environment and other particles have a weak relationship to its magnetization, these other particles will roughly still contain the desired original magnetization. So, a correlation as close to 0 as possible is optimal.

We review an example of the covariance matrix with the Matlab model (appendix A) and thereafter the correlation coefficients. For the noise a normally distributed random variable with standard deviation $0.01||\boldsymbol{\phi}||$ is generated and added to $\boldsymbol{\phi}$. See figure 8 to get an idea of what difference this noise makes in the flux measurements.

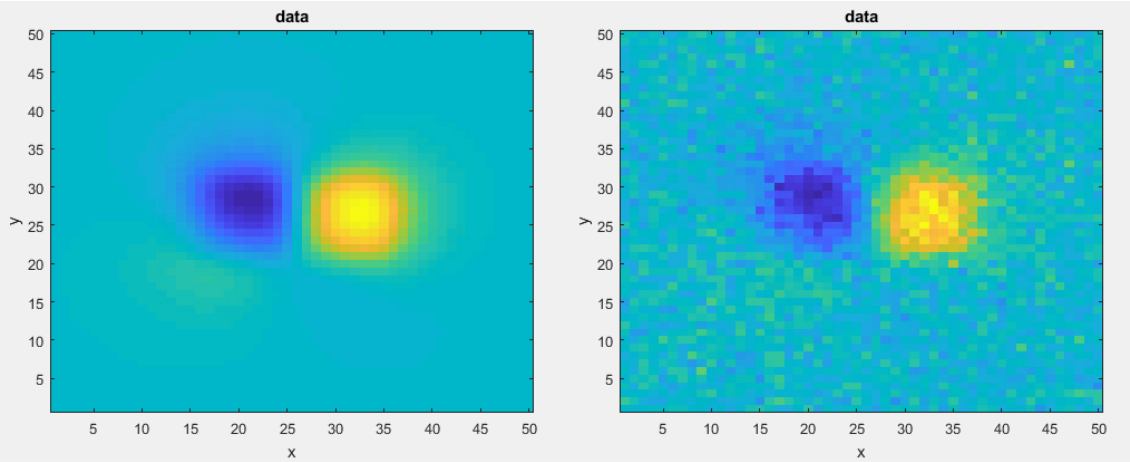

Figure 8: Images of the magnetic field without (left) and with (right) noise. The setup here is the same as in figure 4.

We have two cuboids A and B of equal size ($5 \times 5 \times 5$ µm) located at (-5,0,8) and (5,0,8) with magnetizations $\boldsymbol{m_1} = (1, 3, -2.6)$ and $\boldsymbol{m_2} = (-2, -1.8, 4)$ respectively and a grid of 50×50 sensors with sides of 0.5 µm (like in the previous section). We get the covariance matrix

$$\begin{bmatrix} \mathrm{Var}(\hat{m}_1) & \cdots & \mathrm{Cov}(\hat{m}_1, \hat{m}_{3K}) \\ & \ddots & \vdots \\ & & \mathrm{Var}(\hat{m}_{3K}) \end{bmatrix} = \left[\begin{array}{ccc|ccc} 10 & +0 & -2 & 4 & -0 & 5 \\ & 8 & -0 & +0 & -4 & +0 \\ & & 6 & -5 & +0 & -2 \\ \hline & & & 10 & -0 & 2 \\ & & & & 8 & -0 \\ & & & & & 6 \end{array}\right] \cdot 10^{-3}.$$

As the covariance matrix is symmetric, we only look at the upper triangle for the sake of readability. The values have been rounded off to one significant figure. The zeros are signed to indicate a positive or negative relation before roundoff. The division in the matrix represents

$$\left[\begin{array}{c|c} \mathrm{Var}(\boldsymbol{m_1}) & \mathrm{Cov}(a, b), \text{ where } a \in \boldsymbol{m_1} \text{ and } b \in \boldsymbol{m_2} \\ \hline & \mathrm{Var}(\boldsymbol{m_2}) \end{array}\right].$$

This division comes in handy when looking for specific information; for example information on covariances of the magnetization of only one cuboid is already grouped in the upper left or lower right quarter of the covariance matrix. When K is not 2 but 3, the matrix is divided in 9 by 9 areas, and so forth when K increases.

We translate the covariance matrix into something more comprehensive with the correlation coefficient:

$$\begin{bmatrix} \rho_{11} & \rho_{12} & \rho_{13} & \rho_{14} & \rho_{15} & \rho_{16} \\ & \rho_{22} & \rho_{23} & \rho_{24} & \rho_{25} & \rho_{26} \\ & & \rho_{33} & \rho_{34} & \rho_{35} & \rho_{36} \\ & & & \rho_{44} & \rho_{45} & \rho_{46} \\ & & & & \rho_{55} & \rho_{56} \\ & & & & & \rho_{66} \end{bmatrix} = \left[\begin{array}{ccc|ccc} 1 & +0 & -0.3 & 0.3 & -0 & 0.6 \\ & 1 & -0 & +0 & -0.5 & +0 \\ & & 1 & -0.6 & +0 & -0.3 \\ \hline & & & 1 & -0 & 0.3 \\ & & & & 1 & -0 \\ & & & & & 1 \end{array}\right].$$

As can be seen in the correlation-matrix, the correlations are either 1, in the range of ± 0.3 to ± 0.6 or approximately 0 in this example. Of course, $\rho_{ii} = 1$, as this represents the relationship of magnetization

component $\hat{m}_i$ with itself. With the correlation, we now know for example that when the $z-$component of magnetization of cuboid A ($\hat{m}_3$) increases, the x-component of magnetization of cuboid B ($\hat{m}_4$) decreases quite a lot but its y-component ($\hat{m}_5$) increases only slightly. Of course, it depends on the research when a correlation is considered too high or too low.

4 Application on data of basaltic rock

In the previous chapters, we have described how, in theory, we can determine the individual magnetizations of magnetized particles in a rock sample. A. Béguin put this theory into practice with a synthetic sample she created [2]. This synthetic sample has a low concentration of magnetic particles (132 grains) of which the sizes are known. A. Béguin determined the magnetizations of 23 particles with the inverse model. With a forward model, she could compare these magnetizations per particle with the actual magnetizations. This project lead to the conclusion that the inversion works as desired. The next step is to do this inversion for a natural sample of lava.

4.1 Sample

Here, we use a piece of basaltic rock from the 1907 lava flow on Hawaii (site 3 of de Groot et al. (2013)). Its diameter is 3 mm and it has been polished to a sliver of 30 µm thick (thickness of a typical thin section). Different from the synthetic sample of A. Béguin, is that this sample naturally contains much more magnetized grains (about 70,000/mm^3 [2]) and more different types of particles with a wide variation of properties. The magnetized grains are titanomagnetite, $Fe_{3-x}Ti_xO_4$ [12].

4.2 Information on the particles

A. Béguin and L.V. de Groot prepared the sample and executed the micro-CT scanning. As the magnetite grains in the sample have the highest density of all the materials in the sample, the X-rays of the scanner passing through those grains are most attenuated. This yields micro-CT images in which the lightest areas represent the magnetized grains (figure 9a). As all the tomographic images made are stacked on top of each other, a 3D visualization of the sample is created. The voxel-size (3D-pixels) with which this happens is 0.675x0.675x0.675 µm. With the aid of Avizo, A. Béguin determined the boundaries of the magnetized grains by choosing the gray-scale limit for which an area is considered a magnetized grain or not. Thereafter, the exact locations, sizes and shapes of the grains are determined.
As the particles range in size from 2 to 50 µm in diameter and we work with a voxel-size of 0.675 µm, the particles are represented by about 15 to 200,000 voxels per particle. From the method used (chapter 2), we know that for the measurement of the flux all calculations need to be done for the border of every cuboid, which in this case is every voxel. We need to decrease the amount of calculations, in order to preserve an achievable computation time. For this, the approach of de Groot et al. (2018) is followed: every particle is partitioned into voxel-built cuboids by consecutively generating the largest cuboid that fits in the (non-partitioned) area of the particle. So, the smallest possible cuboids of a particle are the size of one voxel. Now, for each particle we have a clustered group of cuboids representing its shape, size and location (figure 9b).

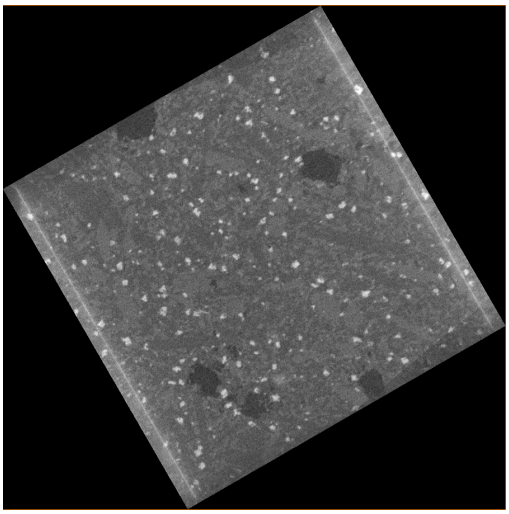

(a) Tomographic image of the sample. The white areas are the magnetized grains.

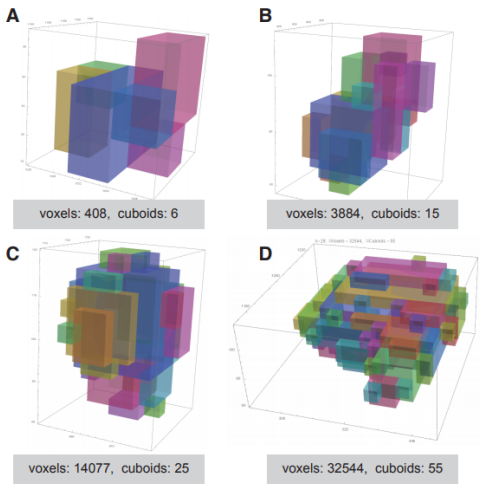

(b) Examples of particles partitioned into cuboids [4].

Figure 9: Information on the particles

4.3 Information on the flux

In chapter 2, we explained how the SQUID-scanner works. The magnetic flux density of this sample, however, is measured with the Quantum Diamond Microscope (QDM) developed by Harvard University (USA) [5]. The QDM has the same resolution as the SQUID scanner and our explanation in chapter 2 regarding the way the flux is being calculated still holds. The QDM is preferred over the SQUID-scanner, because as opposed to the SQUID-scanner it is able to measure the flux at room temperature. Additional to the measurements of the flux, the QDM provides us with a 1440x2400 µm LED image of the surface of the sample (figure 10). After measuring the flux of the sample, an alternating field (AF) of 20 µT is applied, changing its magnetic properties. The QDM scanning is repeated, in order to compare results to see how this alternating field changes the magnetization of the particles.

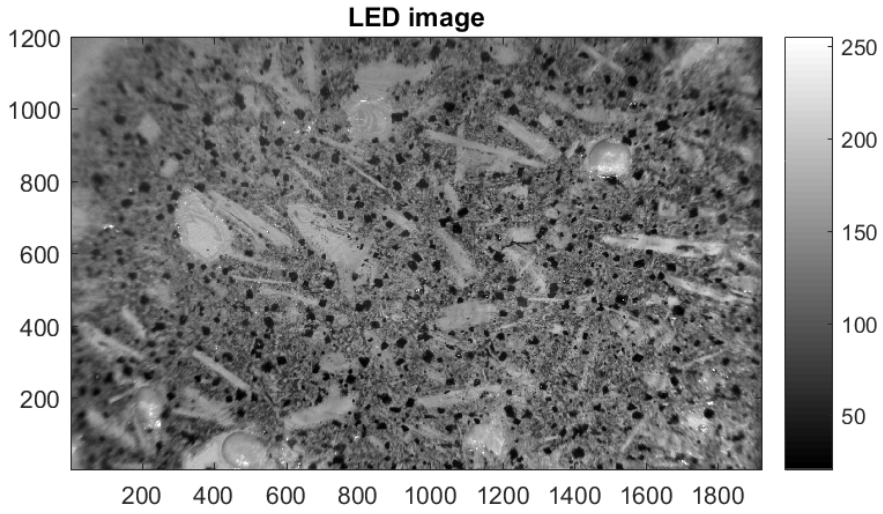

Figure 10: LED image of the sample (before AF), the black areas are the magnetized grains. The Field of View is 1200x2000 steps of 1.2 µm.

4.4 Mapping

The data on the locations, sizes and shapes of the particles need to be mapped with the data on the magnetic flux density of the sample both before and after the appliance of the alternating field. For this mapping, an image of the grains from Avizo is put on top of the LED image and rotated and shifted until they overlap best. With Mathematica, the new coordinates are determined for the LED image by choosing an anchor grain, so that the grains and the magnetic field overlap in the same plane (figure 11).

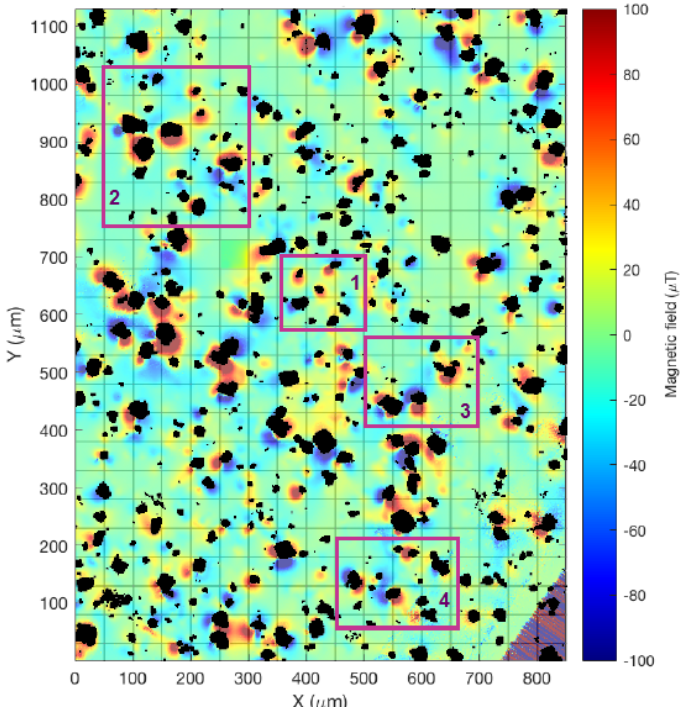

Figure 11: The magnetic field before AF and the grains (black areas) overlapping after mapping, with areas 1 to 4 indicated.

A. Béguin determined 4 areas of interest (figure 11), for each of which the inversion is done. By zooming in on the areas, she found an additional translation is needed to optimize the match between the field and grains. The grains that are only partly within an area are deleted from the data and so not taken into account with the inversion. We obtain areas 1 to 4 which contain 11, 42, 18 and 20 grains and 305, 1192, 388 and 555 cuboids respectively.

4.5 Inversion and results

Areas 1 to 4 are inverted with a Fortran-code written by K. Fabian. In total, the magnetization components of 91 grains are generated, see figures 13 to 16. The magnetizations are the lengths of the magnetization vectors, i.e. $\sqrt{m_x^2 + m_y^2 + m_z^2}$.

The saturated magnetization of magnetite is 480 kA/m [12]; since the magnetizations of the grains are (natural) remanent magnetizations, we expect the magnetizations of the grains to be at maximum 10% of this number. However, the magnetizations generated by the inversion for the original state of the sample range from 184 to 19,876,070 A/m and after the appliance of the AF this range is 126 to 29,335,123 A/m. All grains with a magnetization higher than 48,000 A/m (whether before or after the AF) are excluded from the results (red in figures 13 to 16). We now have with 61 grains with a plausible magnetization. However, magnetizations over 15,000 A/m (about 3% of the saturated magnetization, orange in figures 13 to 16) do not occur very often and so we look at the results after additional exclusion of the grains with magnetization

between 15,000 and 48,000 A/m. We now have 47 grains with a plausible magnetization.
In the tables, the depth is calculated by taking the average of the z-coordinates of the middle points of all the cuboids which constitute the particle in question. Volume is for each particle calculated by adding the volumes of all its cuboids. The change in the last column is calculated by taking the difference between the magnetization before and after appliance of the alternating field, dividing this difference by the original magnetization and multiplying it by 100%. Thus, a change of 100% means the magnetization of that particle has doubled with appliance of the alternating field. A change of -50% means the magnetization of that particle has been halved. The negative percentage of change can not exceed -100%, as then a particle has completely demagnetized.

Taking the average of the magnetizations, we see that overall the magnetizations of the grains become lower after the alternating field is applied (figure 12), which is what we would expect as a demagnetization step was performed. We can also see that including the 14 grains with magnetization between 15,000 and 48,000 A/m yields a much smaller average difference in magnetization than if they are excluded (left and right part of figure 12 respectively). This shows how much influence only a couple of grains with high magnetizations can have on the results.

Averages					
Magnetizations below 48,000 A/m - 61 grains -			Magnetizations below 15,000 A/m - 47 grains -		
original	AF 20 µT	difference	original	AF 20 µT	difference
7713	7556	-157	3688	3242	-446

Figure 12: The averages of the magnetizations.

particle # in Area 1	Depth (µm)	Volume (μm^3)	30µm - Original			30µm - AF20µT			magnetization original	magnetization AF 20 µT	Change %
			mx	my	mz	mx	my	mz			
1	6.8	2380.1	-93.3	-109.4	114.1	287.9	-309.3	172.6	184	456	149
2	18.6	497.9	-3965.4	3680.6	2031.2	-5463.7	530.3	-1651.8	5779	5733	-1
3	22.3	1523.9	3834.2	-1020.5	129.2	-1684.6	26.1	742.3	3970	1841	-54
4	24.1	4411.1	681.2	201.3	2003.0	-545.0	1261.8	-306.3	2125	1408	-34
5	2.7	167.6	31.5	95.6	-358.9	556.5	39.8	1044.9	373	1184	218
6	20.5	239.0	-3139.7	-2280.0	1405.8	5269.8	-2886.9	4177.6	4127	7318	77
7	12.6	892.8	3406.4	-352.8	-2179.7	3337.7	-3912.3	-2537.9	4059	5735	41
8	19.1	524.4	3305.7	-6719.4	-11923.8	1572.4	11192.4	3703.2	14080	11894	-16
9	16.0	1238.5	-5321.0	-5255.9	-5451.1	-6320.9	-5393.8	1316.1	9255	8413	-9
10	32.8	278.6	3923.7	-42684.7	-8728.7	28002.0	-25041.8	1690.8	43744	37604	-14
11	22.5	461.6	11009.5	53579.0	-5083.8	15082.8	2917.7	-9091.1	54934	17851	-68

Figure 13: Obtained magnetizations in A/m of Area 1 before (original) and after (AF 20µT) the appliance of the alternating field. Red color indicates a grain with magnetization over 48,000 A/m, orange color indicates a grain with magnetization between 15,000 and 48,000 A/m.

particle # in Area 2	Depth (µm)	Volume ($µm^3$)	30µm - Original			30µm - AF20µT			magnetization original	magnetization AF 20 µT	Change %
			mx	my	mz	mx	my	mz			
1	2.8	215.9	162.7	117.8	99.1	114.3	-50.6	18.9	224	126	-44
2	6.3	4204.5	-431.3	896.6	-3.9	37.0	292.3	-155.3	995	333	-67
3	25.0	2659.1	1758.6	-82.4	-16084.3	-2800.3	-19799.5	4152.8	16180	20423	26
4	31.8	309.7	11793.8	-9067.7	-10115.0	11687.2	1059.3	-2468.3	17990	11992	-33
5	31.7	346.9	-13733.0	-14889.2	4270.0	-19112.3	-21996.4	484.7	20701	29144	41
6	31.6	3.4	-2398938.7	1531161.9	19671268.5	285733.3	26605403.7	-12353959.0	19876070	29335123	48
7	28.5	2254.6	6551.2	-6857.4	-783.3	-11845.7	1863.3	1800.5	9516	12126	27
8	32.4	9.8	664133.5	649710.5	-704049.2	-723285.9	1792926.3	1703846.4	1165711	2576979	121
9	13.2	1281.5	-147.8	-700.5	-1145.0	1386.0	-2909.6	-1338.1	1350	3490	158
10	3.3	141.5	406.7	-332.8	484.8	89.6	821.8	25.2	715	827	16
11	6.0	4.0	42357.6	81147.0	32565.7	58444.9	38726.0	-11869.6	97157	71108	-27
12	13.3	120.6	-8031.6	15190.7	-17792.6	2723.1	25398.7	-2373.5	24735	25654	4
13	4.0	1821.0	166.5	190.7	-40.9	149.2	406.0	-285.3	256	518	102
14	5.8	1498.4	-630.0	614.5	-69.8	-367.8	105.1	401.1	883	554	-37
15	12.7	8576.6	-563.7	720.9	-774.9	31.8	427.0	-694.2	1199	816	-32
16	27.3	230.0	-93777.3	28060.3	8976.7	-86260.3	81834.4	-66006.8	98296	135995	38
17	22.4	16000.1	-766.9	917.8	-1878.2	-820.1	3005.1	-636.3	2227	3179	43
18	26.5	12.3	-965702.3	-206642.2	-820358.4	1675777.7	62461.0	-219784.3	1283850	1691283	32
19	31.5	11.4	736772.7	1788568.9	219777.9	-2675601.5	1642714.4	7571262.7	1946822	8196424	321
20	15.7	4.6	145568.5	-3057310.7	-7025318.3	-2687427.7	-8716736.4	-6508365.1	7663122	11205471	46
21	13.2	12.6	929288.8	1819826.5	693075.6	1416987.4	2519688.9	784873.2	2157707	2995448	39
22	29.5	186.7	-140959.6	-38910.0	88752.4	182693.0	-9059.4	-164493.5	171057	246002	44
23	17.2	13.8	-56846.6	347911.1	1571367.3	-1084946.8	-624424.3	1125236.7	1610425	1683203	5
24	21.5	283.3	2947.4	-3639.9	-4813.0	-34227.1	5823.3	-1769.0	6716	34764	418
25	5.5	951.2	-80.2	294.8	-7.5	446.1	2.8	0.9	306	446	46
26	7.6	617.2	968.7	-978.1	133.7	-160.2	-707.4	413.7	1383	835	-40
27	19.5	11171.0	13.0	-1029.7	-1723.6	-271.7	-761.8	179.6	2008	828	-59
28	12.2	13407.5	269.1	397.6	-430.4	757.4	542.3	-474.4	645	1045	62
29	30.8	2023.7	-1468.6	-2003.9	10821.4	13465.8	-4389.9	20974.6	11103	25309	128
30	2.7	9.2	1243.6	5850.4	4239.0	3480.3	-1643.3	735.5	7331	3918	-47
31	22.7	737.8	1032.2	-4222.7	-14174.6	-3514.7	4727.9	5418.2	14826	8004	-46
32	19.9	758.1	-762.9	-1218.6	-1808.3	-2409.7	-430.3	175.2	2310	2454	6
33	29.7	6.5	-19095.8	-136834.1	123283.5	-40428.6	-791464.8	286214.9	185168	842597	355
34	28.4	28.3	296327.1	-23009.1	41613.2	489682.0	10667.5	52519.6	300118	492606	64
35	30.4	1546.7	-1818.7	13066.7	7312.4	21563.3	523.3	17429.3	15084	27731	84
36	14.7	950.9	-1036.3	44.0	-4860.8	-2318.2	-603.1	-3056.0	4970	3883	-22
37	22.1	4.3	-1636927.9	598887.5	-697256.2	-1449494.1	478987.8	1184997.9	1877329	1932533	3
38	26.9	1147.8	5072.4	-4441.0	1477.4	3462.5	-4862.5	3654.0	6902	6999	1
39	33.3	4.3	3445324.1	-4423363.6	-1121347.5	-10183459.5	-4942288.0	-7851116.0	5717851	13775670	141
40	10.1	150.4	1789.5	-2790.3	3064.9	3837.7	-1741.7	3326.1	4515	5369	19
41	22.6	2036.0	-2019.4	-636.5	3368.7	-542.9	-34.9	2407.1	3979	2468	-38
42	17.7	188.5	-445.4	-9170.3	422.7	-6130.0	6273.8	-6844.5	9191	11126	21

Figure 14: Obtained magnetizations in A/m of Area 2 before (original) and after (AF 20µT) the appliance of the alternating field. Red color indicates a grain with magnetization over 48,000 A/m, orange color indicates a grain with magnetization between 15,000 and 48,000 A/m.

particle # in Area 3	Depth (µm)	Volume ($µm^3$)	30µm - Original			30µm - AF20µT			magnetization original	magnetization AF 20 µT	Change %
			mx	my	mz	mx	my	mz			
1	10.9	10875.5	-119.3	174.8	-336.5	-160.7	402.9	-165.3	398	464	17
2	7.5	3717.3	722.2	-2408.9	373.3	299.8	-1425.4	-576.8	2542	1567	-38
3	27.4	85.8	-2471.7	235858.5	77791.1	54327.5	-118532.4	-72121.6	248368	149006	-40
4	15.5	50.4	82030.4	-29553.1	-66239.7	-12763.5	-47279.9	-35156.6	109499	60285	-45
5	4.6	180.2	-689.7	1001.6	-228.0	125.5	703.9	345.6	1237	794	-36
6	30.1	248.8	-35021.9	-85866.8	9589.8	-94479.5	166550.3	22928.0	93229	192850	107
7	33.4	8.6	1567320.4	2658542.6	357218.7	4507769.5	-4676700.5	991698.4	3106758	6570767	111
8	11.8	3722.9	-731.4	-1750.7	691.8	260.5	-1962.2	468.2	2019	2034	1
9	27.0	1503.6	15108.0	7083.0	271.9	-4724.4	21424.3	2467.2	16688	22077	32
10	31.3	78.1	133554.4	-11196.1	28369.6	-26786.7	84472.1	-64095.3	136993	109368	-20
11	10.4	12.9	-83222.1	-68708.7	-2027.4	-100534.1	-23889.6	-59006.0	107939	118994	10
12	17.4	586.8	-9460.4	-23900.6	-5701.0	-7319.8	-13837.6	-11918.8	26329	19675	-25
13	23.6	3.7	-556825.7	3738007.5	-2812488.1	191982.2	1841841.5	4292942.9	4710928	4675318	-1
14	25.5	3.4	-1120396.4	-904774.7	-113345.2	6725975.6	-6783303.9	128417.5	1444560	9553452	561
15	3.4	5.8	-2565.7	22684.6	28851.7	-41550.1	20855.5	72236.9	36791	85904	133
16	4.8	4.9	-47000.4	-41163.6	-25396.7	-76021.4	-68957.6	-92314.8	67442	138045	105
17	6.9	2474.8	82.6	-206.3	138.0	271.2	-60.9	-412.9	262	498	90
18	9.1	81.5	13337.1	-13965.3	-5145.7	3250.2	-12740.8	3551.8	19985	13620	-32

Figure 15: Obtained magnetizations in A/m of Area 3 before (original) and after (AF 20µT) the appliance of the alternating field. Red color indicates a grain with magnetization over 48,000 A/m, orange color indicates a grain with magnetization between 15,000 and 48,000 A/m.

particle # in Area 4	Depth (µm)	Volume ($µm^3$)	30µm - Original			30µm - AF20µT			magnetization original	magnetization AF 20 µT	Change %
			mx	my	mz	mx	my	mz			
1	10.0	4319.5	-321.5	111.8	191.9	-666.1	-61.3	385.5	391	772	98
2	31.0	653.5	-6245.6	3344.4	14152.3	-3648.6	11636.3	20075.8	15827	23489	48
3	30.0	1567.6	-5766.4	-7944.2	1025.4	-269.0	-9623.5	1321.4	9870	9717	-2
4	9.1	4553.8	1690.7	141.4	-699.1	388.3	-289.0	-289.9	1835	564	-69
5	33.0	4.9	-1075573.4	-1296627.9	-1311338.8	-5010858.0	-1515690.2	-1493454.2	2134880	5443934	155
6	19.3	449.6	-1798.5	1270.7	7098.0	-1231.0	799.1	5398.4	7432	5594	-25
7	7.9	6031.0	1066.7	-860.5	201.6	402.0	-114.2	214.2	1385	470	-66
8	11.6	173.1	2941.4	974.1	1271.1	600.0	1425.4	3252.9	3349	3602	8
9	8.8	593.3	-2428.8	-1763.2	-290.8	-127.9	-1455.6	105.1	3015	1465	-51
10	5.5	3693.0	604.2	-781.9	294.3	19.8	-461.0	-238.1	1031	519	-50
11	31.7	4.3	2098120.6	753633.3	-1246874.2	-270336.0	-4099447.7	-146656.5	2554363	4110968	61
12	24.8	4428.1	-1220.2	-2012.0	-917.5	1114.8	-356.7	925.2	2526	1492	-41
13	14.7	4.3	-571310.0	1268738.0	640017.1	-514031.3	518620.4	937570.1	1531572	1188374	-22
14	4.0	23.4	3088.2	2921.4	2275.8	996.1	4077.0	782.9	4822	4269	-11
15	31.4	47.7	-111584.8	-94311.0	24378.9	-21792.3	22108.7	578.4	148122	31049	-79
16	19.0	1741.3	-5175.6	5717.9	-7828.5	-3722.0	-563.0	-2900.8	10989	4752	-57
17	2.5	6.2	8191.2	-4713.6	-12301.7	668.4	-4404.1	2708.3	15513	5213	-66
18	7.1	1090.3	389.4	381.7	38.0	-282.2	114.9	-358.0	547	470	-14
19	4.8	6.8	-34603.0	27309.1	15053.0	1213.9	9552.2	-6925.6	46581	11861	-75
20	27.0	7.1	2714851.5	38224.2	1835245.6	3088134.2	-876491.0	-403985.1	3277195	3235431	-1

Figure 16: Obtained magnetizations in A/m of Area 4 before (original) and after (AF 20µT) the appliance of the alternating field. Red color indicates a grain with magnetization over 48,000 A/m, orange color indicates a grain with magnetization between 15,000 and 48,000 A/m.

5 Discussion

5.1 Residue

With the inverse model, the magnetic moment per grain is determined based on the magnetic flux. Then, with the forward model, the flux is determined based on the magnetic moment per grain. We call the difference between the measured flux and the flux calculated by the forward model the residue, see figure 17 for an example. As can be seen in the left image of this figure, there are 4 areas with relatively large residue in the magnetic field: at locations (40, 160), (60, 120), (120, 150) and (210, 100). Looking at the image of the particles in the right of figure 17, these areas of large residue seem to correlate with the locations of the 4 largest particles. An explanation for this can be that the larger particles are not dipoles (as is assumed in the inversion scheme), but multi-domain. When a magnetic particle is multi-domain, it is divided into areas (domains) which each have their own magnetization [12]. Such a particle will not create a smooth magnetic field like a single-domain (dipole) particle. The residue seems to be an expression of multi-domain behavior for which the inversion does not solve. This violates the dipole assumption made in our method.

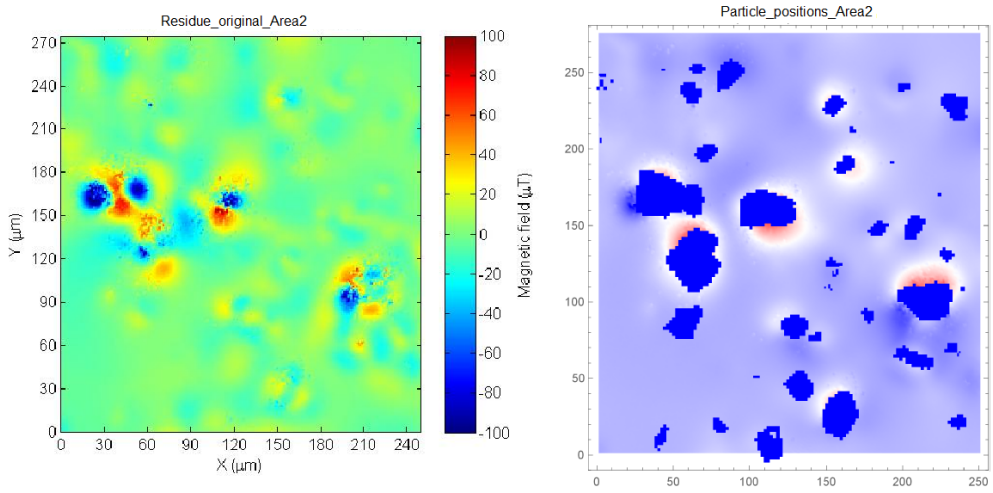

Figure 17: The residue of area 2 (original state) and the locations of the magnetic particles.

5.2 Unreliable magnetizations

From the 91 grains of which the magnetic moment is determined, 44 have a magnetization which is unreliably high (see chapter 4). We look at the locations of these unreliable particles, see figure 18.

As can be seen in figure 18, most of the smaller grains are encircled, only a few are not. It appears that generally speaking the smaller grains are unreliable. Maybe the magnetizations of these particles are affected by the (larger) particles with relatively high magnetization in their neighborhood in some way. The locations of a few small particles which yield a magnetization of reliable magnitude back this up: the grain at (215, 25) in area 4 is reliable and not located near a particle with high magnetization, for example.
Besides the smaller grains being unreliable, it looks like particles which overlap in the z-direction also yield an unreliably high magnetization (x and y coordinates roughly the same, with one grain located below the other). For example overlapping particles at (235, 230) in area 2 are unreliable.

In the tables in chapter 4, it seems the unreliable particles are grouped in some way. The numbering of the particles in the tables is done according to the y-location of the particles. With the results just discussed regarding figure 18, we can now explain these groupings with the argument that particles close to each other are likely to be unreliable. For example, in figure 14 particles 18 to 24 all have an unreliably high magnetization. Amongst those are the 5 in figure 18 encircled small particles of area 2 which are located close to each other with respect to the y-direction.

In future research, we would like to increase the amount of magnetizations determined (preferably of $> 10^6$ magnetic particles) to improve the accuracy of the results. As this will mean measuring thicker samples, the unreliable high magnetizations caused by overlap can cause complications: a thicker sample increases the chance on a high amount of overlapping grains.

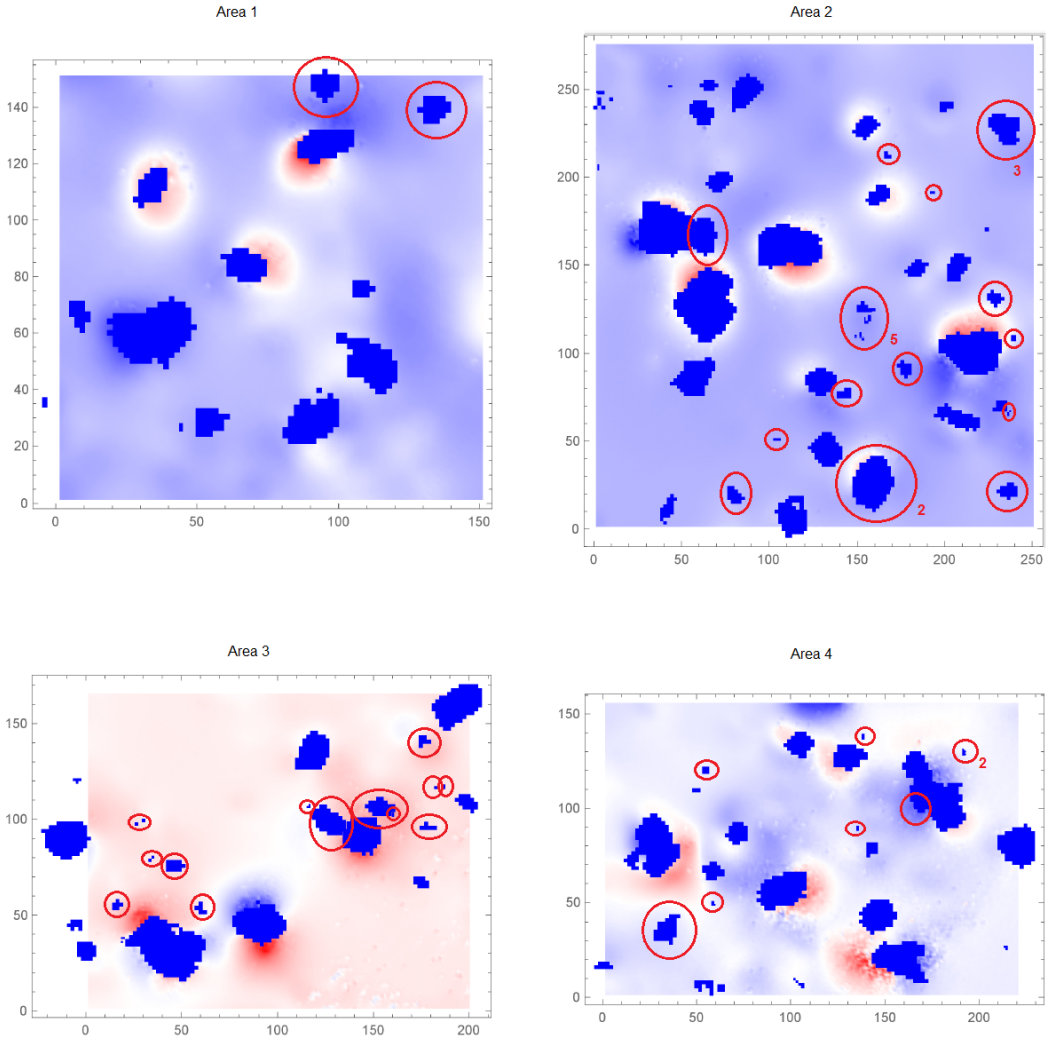

Figure 18: Particles of area 1 to 4, the encircled ones have a magnetization higher than 15,000 A/m either before or after AF and are therefore considered unreliable. A number next to a circle indicates an amount of grouped small particles all with high magnetization or a number of (in z-direction) overlapping particles all with high magnetization.

5.2.1 Vertical overlap: relationship between covariance matrix and inversion result

In chapter 3, we explained how the condition number of the inverse problem tells us something about the stability of the solution: a high condition number means the solution is very sensitive to changes in the initial conditions, whereas a low condition number (the lowest being 1) tells us the solution changes proportionally to change in the initial conditions. In the simple Matlab-example in chapter 3, we saw that overlapping particles in the z-direction gives a relatively high condition number (compared to overlap in the x- or y-direction). In chapter 3, we also explained how the covariance matrix of the solution tells us something about the degree of association between (magnetizations of) particles with the correlation coefficient.

In this chapter, we have just discussed how the inversion results lead us to believe that particles which overlap in the z-direction are unreliable. With the Matlab-model created by T. van Leeuwen (appendix A), we look at the relationship between the covariance matrix and the inversion result when particles overlap in z-direction.

We have cuboids A and B measuring $5 \times 5 \times 5$ µm and a measurement grid of 50×50 sensors with sides of 0.5 µm. Noise is represented by a multivariate normally distributed measurement error $\boldsymbol{\epsilon}$ with standard deviation $0.01||\boldsymbol{\phi}||$. The cuboids are located at (5, 0, 10) and (5, 0, 20) and have magnetizations $\boldsymbol{m_1} = (1.0, 3.0, -2.6)$ and $\boldsymbol{m_2} = (-2.0, -1.8, 4.0)$ respectively. See figure 19. The total magnetization vector is

$$\boldsymbol{m} = \begin{pmatrix} \boldsymbol{m_1} & \boldsymbol{m_2} \end{pmatrix} = \begin{pmatrix} 1.0 & 3.0 & -2.6 & -2.0 & -1.8 & 4.0 \end{pmatrix}.$$

With Matlab, for the inversion result we get

$$\hat{\boldsymbol{m}} = \begin{pmatrix} 1.0 & 2.9 & -2.6 & -2.3 & -1.5 & 4.2 \end{pmatrix}.$$

We can see that the magnetization vectors of cuboid B (which is overlapped by cuboid A) in $\hat{\boldsymbol{m}}$ differ more from the true magnetization than the magnetization vectors of cuboid A in $\boldsymbol{m}$.
The covariance matrix is

$$\sigma^2(Q^TQ)^{-1} = \begin{bmatrix} 5 & 0 & 0 & -20 & 0 & 0 \\ & 5 & 0 & 0 & -20 & 0 \\ & & 3 & 0 & 0 & -8 \\ & & & 80 & 0 & 0 \\ & & & & 80 & 0 \\ & & & & & 40 \end{bmatrix} \cdot 10^{-3}.$$

The only significant relations are the variances of all the magnetization-components and the relations between the two x, y and z-components. The variances of the magnetization-components of cuboid B are way larger than those of cuboid A.
For this situation, the condition number is 9.7. In chapter 3, we discussed how the condition number increases as the cuboids move apart in the z-direction. Moving cuboid B to the deeper location (5, 0, 35), we get a condition number of 20. In this situation, the inversion result is

$$\hat{\boldsymbol{m}} = \begin{pmatrix} 1.0 & 3.0 & -2.5 & -1.4 & -2.5 & 3.4 \end{pmatrix},$$

and the covariance matrix is

$$\sigma^2(Q^TQ)^{-1} = \begin{bmatrix} 4 & 0 & 0 & -20 & 0 & 0 \\ & 4 & 0 & 0 & -20 & 0 \\ & & 2 & 0 & 0 & -8 \\ & & & 500 & 0 & 0 \\ & & & & 500 & 0 \\ & & & & & 200 \end{bmatrix} \cdot 10^{-3}.$$

The magnetization of cuboid A in $\hat{\boldsymbol{m}}$ still does not differ much from $\boldsymbol{m}$. However, the magnetization of cuboid B in $\hat{\boldsymbol{m}}$ differs even more from $\boldsymbol{m}$. The variances of its magnetization-components have increased significantly. The condition number tells us about the sensitivity of the solution, which in the second example has increased with respect to the first situation. However, apparently that sensitivity may only be reflected in a part of the solution, as this increase in sensitivity is only expressed in the magnetization of cuboid B.

If $(Q^TQ)^{-1}$ can be retrieved from the Fortran-code used for our inverse model as in chapter 2, the covariance matrix can be assessed; a comparison can be made between the particles which give high variances in the matrix and the particles which have unreliably high magnetizations as determined by inversion. It would be interesting to see whether there indeed is a clear link between the two, as the simple examples suggest. If so, the covariance matrix may be used in future research to determine which particles are better left out of the inversion scheme. This would decrease computation time and increase the accuracy of results.

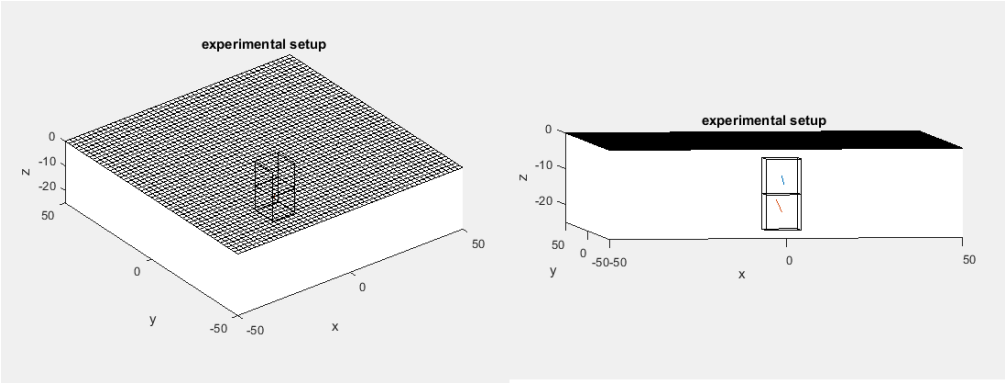

Figure 19: Cuboid A (at (5,0,10)) and B (at (5,0,20)) with magnetization vectors and sensor grid modeled with Matlab. The left and right image give different views of the same setup.

5.3 Particle size

From our results, we deduce that large particles can not be solved reliably due to their multi-domain behavior and small particles can not be solved reliably due to their instability when in the neighborhood of particles with relatively high magnetizations. This leads us to believe there might be a range of particle sizes which is optimal for determining magnetizations by inversion. Excluding the largest and smallest particles in future research may then result in mostly reliable magnetizations, while also decreasing computation time.

5.4 Alternating Field

5.4.1 Relationship change in magnetization and volume

With an alternating field (AF) we have, on average, performed a demagnetization step of the magnetic particles (chapter 4). We expect that larger particles are more sensitive to the alternating field and so demagnetize more, because of their multi-domain magnetization [12]. In figure 20 we see that, overall, these expectations are confirmed: as particle size increases, the decrease of AF magnetization increases in comparison to the original magnetization.

Looking at the difference in A/m between the magnetizations before and after the appliance of the alternating field against volume in figure 21, we see what we discovered in figure 20 confirmed: on average the magnetizations have decreased and the larger the particle, the greater this decrease (notice the scale on the horizontal axis for volume is logarithmic).

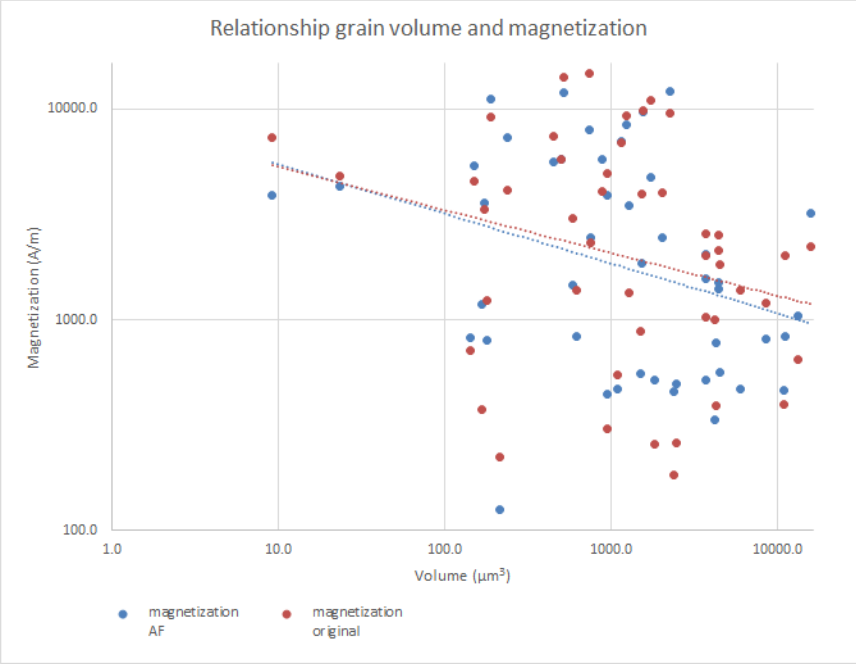

Figure 20: The relationship between grain volume and magnetization indicated by trend lines: red for original magnetization and blue for magnetization after appliance of the alternating field. Only the 47 reliable grains are taken into account.

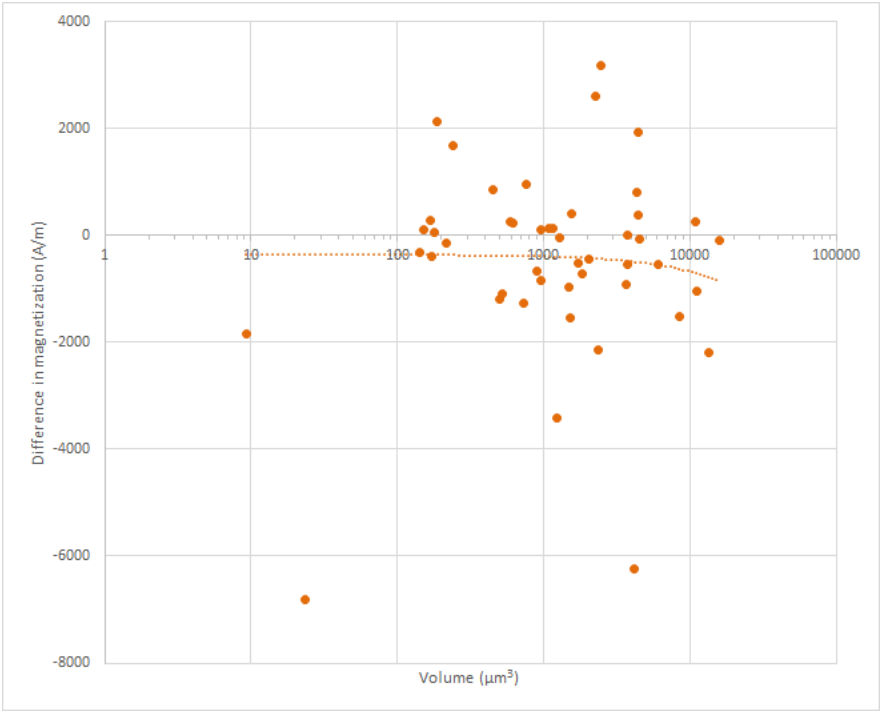

Figure 21: Relationship between the difference in magnetization due to appliance of the alternating field and volume of the particles.

5.4.2 Relationship change in magnetization and depth

In chapter 4, we discussed that 44 of 91 grains are considered unreliable, as their magnetizations determined with the inversion are unrealistically high. In section 5.2 we found that grains which overlap in the z-direction seem to have these high magnetizations and are therefore unreliable. We put the difference in magnetization after appliance of the alternating field of all the grains (both reliable and unreliable) against depth in figure 22.

Notice that the depth in figure 22 exceeds the 30 µm of sample thickness we mentioned in chapter 4. As polishing a sample on such a small scale may not result in the perfect desired thickness, we may assume this explains why some particles are located slightly deeper than 30 µm. The scale for difference on the vertical axis is logarithmic. The differences are absolute values, so this graph does not tell whether a particle has either increased or decreased in magnetization due to the alternating field.

In figure 22, we see that most unreliable grains are located at relatively great depth of the sample. In section 5.2 we discussed how the inversion results suggest that particles which overlap in z-direction yield unreliable magnetizations. With the Matlab model, we considered two examples: one where two cuboids are located directly on top of each other and one where the bottom cuboid is moved to greater depth (see section 5.2 for specifics). The magnetization generated by inversion for both situations shows how the magnetization of cuboid A (the one closest to the surface) does not increase or decrease significantly between the two situations while the magnetization of cuboid B does. This might indicate that only the particles which are overlapped by another particle suffer from this overlap. The magnetization of the particle closer to the surface seems to not be affected substantially by its down neighbor. This theory agrees with figure 22: particles located at greater depth in the sample have more chance of being overlapped by other particles and therefore are more likely to yield unreliably high magnetizations.

The initial thought in section 5.2 is that overlapping grains yield unreliable magnetizations, where no distinction is made between the deeper and shallower ones. For future research, this can be problematic as in that case none of the particles which have another particle located above or below it yield a reliable magnetization. Now, it seems that of the overlapping particles the shallower ones give a reliable magnetization after all, reducing the complications for further research. As the grains between 25 and 35 µm in figure 22 are almost all unreliable, 25 to 30 µm may be the maximum depth at which the magnetizations of grains can reliably be inverted.

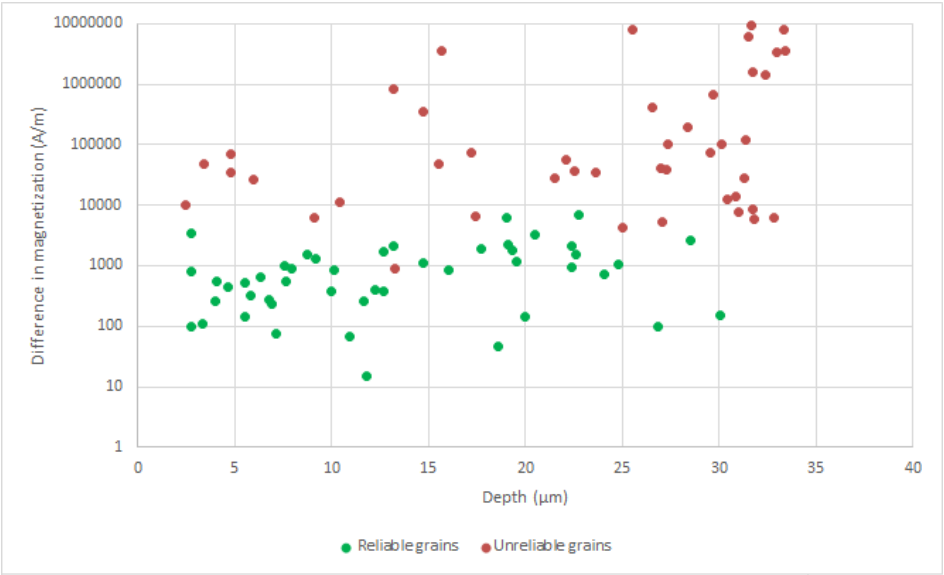

Figure 22: The relationship between difference in magnetization due to appliance of the alternating field and the depth of the particle in the sample. The red dots represented the 44 particles considered unreliable because of unrealistically high magnetizations (chapter 4), the green dots represent the remaining 47 particles.

We can see in figure 22 that the highest differences are also the unreliable ones. In chapter 4 we explained that magnetizations over 15,000 A/m are considered too high to be realistic and thus these particles are considered unreliable. So, only a small percentage of change (see percentages of change in figures 13 to 16 in chapter 4) in the magnetization of an unreliable particle gives a relatively high difference in A/m compared to this same percentage for a reliable particle, which has a lower magnetization. The fact that the unreliable particles in figure 22 have the highest difference in magnetization is therefore logically explained.

5.5 Interpretations, choices and assumptions

In chapter 4, we explained that the boundaries of the grains are determined by choosing a gray-scale limit for which an area in the visualization created by the CT-scanner is considered a grain or not. This is done with Avizo by looking at the areas, changing the gray-scale and choosing for which scale the boundaries are best represented. This technique is not foolproof as it depends on human interpretation rather than exact science, so the chosen boundaries can be off by a few voxels. In chapter 2, we explained how the flux is calculated with, among other things, information on the boundaries of the cuboids constituting the magnetic particles. If the boundaries of a particle are off by a few voxels, then the boundaries of its cuboids are off and as a result, $\boldsymbol{m}$ is less of a best-fit solution.

The mapping of the CT- and QDM-data is done by placing the Avizo-image of the CT-data on top of the QDM LED-image, choosing an anchor grain en rotating and shifting the LED-image until the grains overlap best with the magnetic field (chapter 4). Again, this technique depends on interpretation, which means the mapping can probably be optimized by using a computer program for it.

Assumptions were made regarding the rank of Q and the distribution of the error $\boldsymbol{\epsilon}$. In chapter 3, we state that it can be assumed Q has full column rank, which leads to the conclusion that we have $\boldsymbol{\phi} = (Q^TQ)^{-1}\boldsymbol{m}$, which is what is used in the Fortran-code to determine $\boldsymbol{m}$. With Q being full column rank, we can compute the covariance matrix as $\sigma^2(Q^TQ)^{-1}$. In chapter 3, we also state that the measurement error $\boldsymbol{\epsilon}$ caused by noise is multivariate normally distributed. It is important to realize these assumptions could be false, in which case corrections in the methods used should be made accordingly. However, the chance that $P \leq 3K$ is very small, as can be seen with the following calculation:

> The Field of View of the QDM is 1200×2000 (in steps of 1.2 µm) so for the amount of measurement points we have $P = 2,400,000$. Our sample has been polished to a typical thin section of 30 µm thickness and the Field of View measures 1440×2400 µm. The total volume of lava for which the flux is measured is therefore $103,600,000$ µm^3. As lava contains on average 7 magnetic particles per 100,000 µm^3, we expect to have about $K = 7300$ magnetic particles in the volume. Then, $3K = 22,000$ and so $P \gg 3K$

Even when a sample contains 10 times the amount of magnetic particles of an average sample, P is still way larger than $3K$. For Q to have full column rank, we must have, besides $P > 3K$, columns which are all linearly independent. If they are not, a minimum norm solution can be found with the SVD to approximate $\boldsymbol{m}$ [1].

6 Conclusion

We understand how micromagnetic tomography works and have applied it to a natural sample of magnetic rock. Discussing inverse theory and examining the results of inversion has lead to conclusions of which some are backed up by modeling simple example situations.

A linear inverse model $\boldsymbol{\phi} = Q\boldsymbol{m}$ is found with data on both the particles in a rock sample (shapes, sizes, locations) and on the sensors used for measuring the magnetic flux density (amount, sizes, locations). In general, Singular Value Decomposition can be used to find the pseudo-inverse of the linear operator, yielding a unique solution for an inverse model. For the inverse model in micromagnetic tomography, assuming we have more measurement points than magnetic particles and the linear operator Q has full rank, a solution for $\boldsymbol{m}$ is found with least squares approximation. This solution applies a special case of the pseudo-inverse and is therefore unique.

Assuming noise will cause a measurement error, the condition number indicates the sensitivity of the solution of the inverse model to this noise. Assuming the error is multivariate normally distributed, the covariance matrix of the inverse result $\hat{\boldsymbol{m}}$ can be found with Q and the variance of the error. However, the variance of the error is a scalar by which every element in the matrix is multiplied, so this variance is not necessary for interpreting the relations between the magnetization-components. It seems a sensitive solution (high condition number) implies only some particles are sensitive; only the variances of the magnetization-components of these particles are very high, as expressed in the covariance matrix. In future research, the covariance matrix may be used to determine which particles are sensitive and therefore unreliable and unwanted, in order to filter these out.

The inversion results from applying micromagnetic tomography to a natural sample of basaltic rock suggest that particles which are located deep in the sample are unreliable. Also, both these results and a simple Matlab-model suggest that particles which are overlapped vertically yield unreliable magnetizations. It seems that at this stage, research with micromagnetic tomography can only be done using samples with a maximum thickness of about 25-30 µm: increasing the thickness of the sample only increases the number of particles which are highly likely to be overlapped by other particles, which does not significantly increase the amount of reliable particles (but does increase computation time).

By applying an alternating field to the sample of lava and repeating the inversion with new flux measurements, a relation between particle size and decrease in magnetization was found: the larger a particle, the more decrease in magnetization due to appliance of the alternating field. In the inversion scheme, it is assumed that particles are dipoles. However, the fact that larger particles demagnetize more suggests they are multi-domain (which is generally the case for larger particles [12]). Also, the residue in the magnetic field found with the forward model correlates with particle size, again confirming multi-domain behavior of the larger particles. As in general small particles are unreliable, it seems there is a size range for which the inversion works optimally.

Improving the accuracy of input data will improve the accuracy of the inversion result in future research. Computer programs in stead of human interpretation may be used for determining boundaries of the grains in the CT-data and for mapping the data sets on the particles and the flux measurements. This will probably yield more accurate magnetizations generated by inversion.

A Matlab code

Written by T. van Leeuwen.

```
function A = getMatrix(sensors, cuboids)
% Construct weight matrix for forward modelling of SQUID measurements, see
% [reference]
%
% use:
%   A = getMatrix(sensors, cuboids)
%
% input:
%   sensors -  p x 5 array where each row [xs,ys,zs,dx,dy] describes a sensor
%   cuboids -  k x 6 array where each row [xc, yc, zc, a, b, c] describes a cuboid
%
% output:
%   A - p x 3k matrix

% sizes
P = size(sensors,1);
K = size(cuboids,1);

% initialize matrix
A = zeros(P,3*K);

% fill matrix
for k = 1:P
    % sensor parameters
    xs = sensors(k,1); ys = sensors(k,2); zs = sensors(k,3); dx = sensors(k,4); dy = ...
        sensors(k,5);

    for l = 1:K
        % cuboid parameters
        x = cuboids(l,1); y = cuboids(l,2); z = cuboids(l,3); a = cuboids(l,4); b = ...
            cuboids(l,5); c = cuboids(l,6);

        % weight for Mx, equation (5) of supplementary material of [1]
        A(k,3*(l-1) + 1)     = Fx(x - xs, y - ys, z - zs, dx, dy, a, b, c);
        % weight for My
        A(k,3*(l-1) + 2) = Fy(x - xs, y - ys, z - zs, dx, dy, a, b, c);
        % weight for Mz
        A(k,3*(l-1) + 3) = Fz(x - xs, y - ys, z - zs, dx, dy, a, b, c);

    end
end
end

function val = Fx(x, y, z, dx, dy, a, b, c)
    f = @(xt,yt,zt,xtt,ytt) F120(x + xt - xtt, y + yt - ytt, z + zt);
    val = integr(f,a,b,c,dx,dy);
end

function val = Fy(x, y, z, dx, dy, a, b, c)
    f = @(xt,yt,zt,xtt,ytt) F210(x + xt - xtt, y + yt - ytt, z + zt);
    val = integr(f,a,b,c,dx,dy);
end

function val = Fz(x, y, z, dx, dy, a, b, c)
    f = @(xt,yt,zt,xtt,ytt) F211(x + xt - xtt, y + yt - ytt, z + zt);
    val = integr(f,a,b,c,dx,dy);
end

function val = F120(x,y,z)
    r = sqrt(x.^2 + y.^2 + z.^2);
    Az = atan((x.*y)./(z.*r));
    Lx = log(x + r);
    Ly = log(y + r);
```

```
62
63      val = -0.5*r.*x - y.*z.*Az + x.*y.*Ly + 0.5*(y.^2 - z.^2).*Lx;
64  end
65
66  function f = F210(x,y,z)
67      r = sqrt(x.^2 + y.^2 + z.^2);
68      Az = atan((x.*y)./(z.*r));
69      Lx = log(x + r);
70      Ly = log(y + r);
71
72      f = -0.5*r.*y - x.*z.*Az + x.*y.*Lx+ 0.5*(x.^2 - z.^2).*Ly;
73  end
74
75  function val = F211(x,y,z)
76      r = sqrt(x.^2 + y.^2 + z.^2);
77      Az = atan((x.*y)./(z.*r));
78      Lx = log(x + r);
79      Ly = log(y + r);
80
81      val = -x.*y.*Az - x.*z.*Lx - y.*z.*Ly + z.*r + x.*y.*z.*(x./(x.^2 + z.^2) + y./(y.^2 + ...
            z.^2));
82  end
83
84  function val = integr(f,a,b,c,dx,dy)
85      val = 0;
86      for i = [-1,1]
87          for j = [-1,1]
88              for k = [-1,1]
89                  for l = [-1,1]
90                      for m = [-1,1]
91                          val = val + i*j*k*l*m*f(i*a, j*b, k*c, l*dx, m*dy);
92                      end
93                  end
94              end
95          end
96      end
97  end
```

```
1   function plotSetup(sensors,cuboids,magnetization)
2
3   % sizes
4   P = size(sensors,1);
5   K = size(cuboids,1);
6
7   plot_magnetization = 0;
8   if nargin == 3
9       magnetization = reshape(magnetization,3,K);
10      plot_magnetization = 1;
11  end
12
13
14  for k = 1:P
15      % sensor parameters
16      xs = sensors(k,1); ys = sensors(k,2); zs = sensors(k,3); dx = sensors(k,4); dy = ...
            sensors(k,5);
17      draw_square(xs,ys,-zs,dx,dy);
18
19  end
20
21  for l = 1:K
22      % cuboid parameters
23      x = cuboids(l,1); y = cuboids(l,2); z = cuboids(l,3); a = cuboids(l,4); b = ...
            cuboids(l,5); c = cuboids(l,6);
24      draw_cuboid(x,y,-z,a,b,c);
25
26      if plot_magnetization
```

```
        hold on;quiver3(x,y,-z,magnetization(1,l),magnetization(2,l),magnetization(3,l));
    end

end
%zt = get(gca, 'ZTick');
%set(gca, 'ZTick', zt, 'ZTickLabel', -zt)

function draw_square(xs,ys,zs,dx,dy)
    vert = [xs + dx ys + dy zs; xs + dx ys - dy zs; xs - dx ys - dy zs; xs - dx ys + dy zs];
    faces = [1 2 3 4];

    patch('Faces',faces,'Vertices',vert,'Facecolor','none');

end

function draw_cuboid(xs,ys,zs,dx,dy,dz)
    vert = [
        xs - dx ys - dy zs - dz;
        xs + dx ys - dy zs - dz;
        xs + dx ys + dy zs - dz;
        xs - dx ys + dy zs - dz;
        xs - dx ys - dy zs + dz;
        xs + dx ys - dy zs + dz;
        xs + dx ys + dy zs + dz;
        xs - dx ys + dy zs + dz];
    fac = [1 2 6 5;2 3 7 6;3 4 8 7;4 1 5 8;1 2 3 4;5 6 7 8];
    patch('Vertices',vert,'Faces',fac,'FaceColor','none')

end

end
```

```
% define sensor grid of 50 x 50 sensors of size dx = dy = 0.5 at z = 0
p  = 50;
dx = 0.5;
dy = 0.5;
xs = linspace(-dx*(p-1),dx*(p-1),p);
ys = linspace(-dy*(p-1),dy*(p-1),p);
zs = 0;

[xxs, yys] = meshgrid(xs,ys);

sensors = [xxs(:), yys(:), zs*ones(p^2,1), dx*ones(p^2,1), dy*ones(p^2,1)];

% define two cuboids of size 5 x 5 x 5 centered at (-5,0,8) and (5, 0, 8)
cuboids = [-5,0,8,5,5,5; 5,0,8,5,5,5];

% get matrix, compute data
Q = getMatrix(sensors, cuboids);
m = [1;3;-2.6;-2;-1.8;4]; % [m1x,m1y,m1z,m2x,m2y,m2z]
phi = Q*m;
e = normrnd(0,0.01*norm(phi),size(phi));
phi = phi+e;

% invert (pseudo-inverse)
mest = lsqr(Q,phi);

% plot
figure(1)
plotSetup(sensors,cuboids,m);axis equal tight;view(3)
title('experimental setup')
xlabel('x')
ylabel('y')
zlabel('z')

figure(2)
```

```
35 imagesc(reshape(phi,p,p)); axis xy
36 title('data')
37 xlabel('x')
38 ylabel('y')
39
40 figure(3)
41 plotSetup(sensors,cuboids,mest);axis equal tight;view(3)
42 title('reconstruction')
43 xlabel('x')
44 ylabel('y')
45 zlabel('z')
```

References

[1] U. M. Ascher and C. Greif, *A First Course in Numerical Methods*, Society for Industrial and Applied Mathematics, Philadelphia, 1 ed., 2011.

[2] A. Béguin, *Micromagnetic tomography in practice*, master's thesis, Utrecht University, 2016.

[3] L. V. de Groot, A. J. Biggin, M. J. Dekkers, C. G. Langereis, and E. Herrero-Bervera, *Rapid regional perturbations to the recent global geomagnetic decay revealed by a new hawaiian record.*, Nature Communications, (2013), https://doi.org/10.1038/ncomms3727.

[4] L. V. de Groot, K. Fabian, A. Béguin, P. Reith, A. Barnhoorn, and H. Hilgenkamp, *Determining individual particle magnetizations in assemblages of micro-grains.* Geophysical Research Letters, 2018, https://agupubs.onlinelibrary.wiley.com/doi/abs/10.1002/2017GL076634, https://arxiv.org/abs/https://agupubs.onlinelibrary.wiley.com/doi/pdf/10.1002/2017GL076634.

[5] D. R. Glenn, R. R. Fu, P. Kehayias, D. Le Sage, E. A. Lima, B. P. Weiss, and R. L. Walsworth, *Micrometer-scale magnetic imaging of geological samples using a quantum diamond microscope*, 2017.

[6] G. H. Golub and C. F. V. Loan, *Matrix computations*, vol. 3, JHU Press, 2012.

[7] J. Hadamard, *Sur les problèmes aux dérivées partielles et leur signification physique*, Princeton University Bulletin, (1902), pp. 49–52.

[8] H. A. Haus and J. R. Melcher, *Electromagnetic fields and energy.* Massachusetts Institute of Technology: MIT OpenCourseWare, http://ocw.mit.edu, 1989. Last accessed 11/05/2018. License: Creative Commons Attribution-NonCommercial-Share Alike.

[9] J.Hadamard, *Le problème de Cauchy*, Hermann, 1932.

[10] C. D. Meyer, *Matrix analysis and applied linear algebra*, vol. 71, Siam, 2000.

[11] R. Penrose, *A generalized inverse for matrices*, in Mathematical proceedings of the Cambridge philosophical society, vol. 51, Cambridge University Press, 1955, pp. 406–413.

[12] L. Tauxe, S. K. Banerjee, R. F. Butler, and R. van der Voo, *Essentials of Paleomagnetism*, 4th Web Edition, 2016, https://earthref.org/MagIC/books/Tauxe/Essentials/.

[13] L. Wasserman, *All of statistics: a concise course in statistical inference*, Springer Science & Business Media, 2013.